

Fine-grained Optimization of Deep Neural Networks

Mete Ozay, *Member, IEEE*

Abstract

In recent studies, several asymptotic upper bounds on generalization errors on deep neural networks (DNNs) are theoretically derived. These bounds are functions of several norms of weights of the DNNs, such as the Frobenius and spectral norms, and they are computed for weights grouped according to either input and output channels of the DNNs. In this work, we conjecture that if we can impose multiple constraints on weights of DNNs to upper bound the norms of the weights, and train the DNNs with these weights, then we can attain empirical generalization errors closer to the derived theoretical bounds, and improve accuracy of the DNNs.

To this end, we pose two problems. First, we aim to obtain weights whose different norms are all upper bounded by a constant number, e.g. 1.0. To achieve these bounds, we propose a two-stage renormalization procedure; (i) normalization of weights according to different norms used in the bounds, and (ii) reparameterization of the normalized weights to set a constant and finite upper bound of their norms. In the second problem, we consider training DNNs with these renormalized weights. To this end, we first propose a strategy to construct joint spaces (manifolds) of weights according to different constraints in DNNs. Next, we propose a fine-grained SGD algorithm (FG-SGD) for optimization on the weight manifolds to train DNNs with assurance of convergence to minima. Experimental results show that image classification accuracy of baseline DNNs can be boosted using FG-SGD on collections of manifolds identified by multiple constraints.

I. INTRODUCTION

Despite the practical success of DNNs, understanding their generalization behavior is certainly an open problem [1]. The recent theoretical works [2], [3], [4], [5], [6], [7], [8] addressed this problem by extending the early results proposed for shallow linear neural networks (NNs) [9] for a more general class of DNNs (e.g. NNs with ReLU) and convolutional neural networks (CNNs) (see Table VI for a comparison). The proposed asymptotic bounds were obtained by defining matrices of weights of DNNs using random matrices, and applying concentration inequalities on them. Thereby, the bounds were computed by functions of several ℓ_p norms of matrices of weights, where $1 \leq p \leq \infty$.

In this work, we conjecture that if we can impose multiple constraints on weights of DNNs to set upper bounds of the norms of the weight matrices, and train the DNNs with these weights, then the DNNs can achieve empirical generalization errors closer to the proposed theoretical bounds, and we can improve their accuracy in various tasks. We pose two problems in order to achieve this goal; (1) renormalization of weights to upper bound norms of their matrices, (2) training DNNs with renormalized weights with assurance to convergence to minima.

(1) Bounding norms of weights: We propose a two-stage renormalization procedure. First, we normalize weights according to the Euclidean, Frobenius and spectral norm, since they are used in the bounds of generalization errors [2], [3], [4], [5], [6], [7], [8]. Second, we aim to reparameterize the normalized weights to set a finite and constant upper bound on the weight matrices. For this purpose, we can use a parameter learning approach as utilized in batch normalization (BN) [10]. However, such an approach substantially increases running time of DNNs during training. In addition, it is not efficient to estimate the parameters using small number of samples in batch training. Therefore, we reparameterize weights according to (a) geometric properties of weight spaces, and (b) statistical properties of features (standard deviation) on which the weights are applied. The proposed reparameterization method enables to set upper bound of each different norm of weight matrices to 1.0. In addition, the proposed renormalization procedure enables to control variance of weights during training of DNNs, thereby assures that DNNs do not have spurious local minima [11]. Employment of standard deviation in reparameterization also makes optimization landscapes significantly smoother by bounding amount of change of norms of gradients during training. This property has been recently studied to analyze effect of BN on optimization landscape

in [12]. We use this property to develop a new optimization method for weight renormalization in this paper, as explained in the next problem.

(2) Training DNNs with renormalized weights: We consider two subproblems. (i) First, note that, there is not a single procedure used to normalize weights jointly according to all different norms. Thereby, we normalize weights in groups such that similar or different norms can be used to normalize matrices of weights belonging to each different group. We can mathematically prove that the procedure proposed to solve the previous problem (1) can set an upper bound for all of the aforementioned norms. However, we do not have a mathematical proof to explain whether weights normalized according a single norm can provide the best generalization bound, and to determine its type. We examine this question in various experiments in detail in the supp. mat. Experimental results show that training DNNs using a set of groups of weights normalized according to all these different norms achieves the best generalization performance in various tasks. Since we cannot mathematically verify this observation, we conjecture that using a diverse set of weights normalized with different constraints improves the generalization error compared to using weights normalized according to single constraint. We consider mathematical characterization of this property as an open problem.

Spaces of normalized weights can be identified by different Riemann manifolds [13]¹; (i) unit norm weights reside on the sphere $Sp(A_l B_l - 1)$, (ii) orthonormal weights belong to the Stiefel manifold $St(A_l, B_l)$, and (iii) weights with orthogonal columns reside on the oblique manifold $Ob(A_l B_l)$, at each l^{th} layer of a DNN. We consider training DNNs using a more general setting employing groups of weights which can be normalized according to different normalization constraints. Group wise operations are implemented by concatenating weight matrices $\omega_{g,l}^i$ belonging to each g^{th} group by $\omega_{g,l} = (\omega_{g,l}^1, \omega_{g,l}^2, \dots, \omega_{g,l}^g), \forall g = 1, 2, \dots, G_l$. For the corresponding group, a space of concatenated weights is identified by Cartesian product of manifolds of weights $\omega_{g,l}^i, i = 1, 2, \dots, g$. In addition, if we renormalize weights using standard deviation of features obtained at each epoch, then geometry of the manifolds of weights also changes. Therefore, we address the second subproblem (ii) which is optimization on dynamically changing product manifolds of renormalized weights.

DNNs can be trained with multiple constraints using optimization methods proposed for training shallow algorithms [14], [15], and individual manifolds [13], [16]. If we employ these methods on products of weight manifolds (POMs) to train DNNs, then we observe early divergence, vanishing and exploding gradients due to nonlinear geometry of product of different manifolds. More precisely, the assumption of a bound on the operator norm of Hessian of geodesics in POMs, which is required for assurance of convergence, fails, while performing Stochastic Gradient Descent (SGD) with backpropagation on product of different weight manifolds. Therefore, a non-increasing bound on the probability of failure of the optimization algorithm cannot be computed, and a convergence bound cannot be obtained. In order to solve these problems, we first propose a mathematical framework to make use of the geometric relationship between weight manifolds determined by different constraints (Section III). Then, we suggest an approach for training DNNs using multiple constraints on weights to improve their performance under the proposed framework. To this end, we propose a new algorithm that we call fine-grained stochastic gradient descent (FG-SGD) to train DNNs using POMs. We elucidate geometric properties of POMs to assure convergence of FG-SGD to global minima while training nonlinear DNNs with particular assumptions on their architectures, and to local minima while training a more generic class of nonlinear DNNs. Our contributions are summarized as follows:

1) DNNs trained using weights renormalized by the proposed method (see Proposition 1 in the supp. mat. for derivation) can achieve tighter bounds for theoretical generalization errors compared to using unnormalized weights. These DNNs do not have spurious local minima [11] (see the next section for a detailed discussion). The proposed scaling method generalizes the scaling method proposed in [17] for weight normalization by incorporating geometric properties of weight manifolds.

¹Please see the supplemental material for more precise mathematical definitions and examples.

- 2) We explicate the geometry of weight manifolds defined by multiple constraints in DNNs. For this purpose, we explore the relationship between geometric properties of POMs (i.e. sectional curvature), gradients computed at POMs (Theorem 1), and those of component manifolds of weights in DNNs in Section III (please see Lemma 1 in the supp. mat. for more precise results).
- 3) We propose an algorithm (FG-SGD) for optimization on different collections of POMs (Section III) by generalizing SGD methods employed on weight manifolds [13], [18]. Next, we explore the effect of geometric properties of the POMs on the convergence of the FG-SGD using our theoretical results. In the proof of convergence theorems, we observe that gradients of weights should satisfy a particular normalization requirement and we employ this requirement for adaptive computation of step size of the FG-SGD (see (5) in Section IV-A). To the best of our knowledge, this is first result which also establishes the relationship between norms of weights and norms of gradients for training DNNs. We also provide an example for computation of a step size function for optimization on POMs identified by the sphere (Corollary 2 in the supp. mat.).
- 4) We propose a strategy to construct sets of identical and non-identical weight spaces according to their employment in groups on input and output channels in DNNs (Section II). In the experimental analyses, we apply this strategy to train state-of-the-art networks (e.g. Resnext [19], Mobilenetv2 [20] and DeepRoots [21]) which use well-known weight grouping strategies, such as depth-wise or channel-wise grouping, for efficient implementation of DNNs. The results show that the proposed strategy also improves accuracy of these DNNs.
- 5) We prove that loss functions of DNNs trained using the proposed FG-SGD converges to minima almost surely (see Theorem 2 and Corollary 1 in the supp. mat.). To the best of our knowledge, our proposed FG-SGD is the first algorithm performing optimization on different collections of products of weight manifolds to train DNNs with convergence properties.

II. CONSTRUCTION OF SETS OF POMs IN DNNs

Let $S = \{s_i = (\mathbf{I}_i, y_i)\}_{i=1}^N$ be a set of training samples, where y_i is a class label of the i^{th} image \mathbf{I}_i . We consider an L -layer DNN consisting of a set of tensors $\mathcal{W} = \{\mathcal{W}_l\}_{l=1}^L$, where $\mathcal{W}_l = \{\mathbf{W}_{d,l} \in \mathbb{R}^{A_l \times B_l \times C_l}\}_{d=1}^{D_l}$, and $\mathbf{W}_{d,l} = [W_{c,d,l} \in \mathbb{R}^{A_l \times B_l}]_{c=1}^{C_l}$ is a tensor² of weight matrices $W_{c,d,l}, \forall l = 1, 2, \dots, L$, for each c^{th} channel $c = 1, 2, \dots, C_l$ and each d^{th} weight $d = 1, 2, \dots, D_l$. In popular DNNs, weights with $A_l = 1$ and $B_l = 1$ are used at fully connected layers, and those with $A_l > 1$ or $B_l > 1$ are used at convolutional layers. At each l^{th} layer, a feature representation $f_l(\mathbf{X}_l; \mathcal{W}_l)$ is computed by compositionally employing non-linear functions by

$$f_l(\mathbf{X}_l; \mathcal{W}_l) = f_l(\cdot; \mathcal{W}_l) \circ f_{l-1}(\cdot; \mathcal{W}_{l-1}) \circ \dots \circ f_1(\mathbf{X}_1; \mathcal{W}_1), \quad (1)$$

where $\mathbf{X}_l = [X_{c,l}]_{c=1}^{C_l}$, and $\mathbf{X}_1 := \mathbf{I}$ is an image at the first layer ($l = 1$). The c^{th} channel of the data matrix $X_{c,l}$ is convolved with the kernel $W_{c,d,l}$ to obtain the d^{th} feature map $X_{c,l+1} := q(\hat{X}_{d,l})$ by $\hat{X}_{d,l} = W_{c,d,l} * X_{c,l}, \forall c, d, l$, where $q(\cdot)$ is a non-linear function, such as ReLU³.

Previous works [13], [18] employ SGD using weights each of which reside on a single manifold⁴ at each layer of a DNN. We extend this approach considering that each weight can reside on an individual manifold or on collections of products of manifolds, which are defined next.

Definition 1 (Products of weight manifolds and their collections). Suppose that $\mathcal{G}_l = \{\mathcal{M}_{\iota,l} : \iota \in \mathcal{I}_{\mathcal{G}_l}\}$ is a set of weight manifolds⁴ $\mathcal{M}_{\iota,l}$ of dimension $n_{\iota,l}$, which is identified by a set of indices $\mathcal{I}_{\mathcal{G}_l}, \forall l = 1, 2, \dots, L$. More concretely, $\mathcal{I}_{\mathcal{G}_l}$ contains indices each of which represents an identity number (ι) of a weight that resides on a manifold $\mathcal{M}_{\iota,l}$ at the l^{th} layer. In addition, a subset $\mathcal{I}_l^g \subseteq \mathcal{I}_{\mathcal{G}_l}, g = 1, 2, \dots, G_l$, is used to determine a subset $\mathcal{G}_l^g \subseteq \mathcal{G}_l$ of weight manifolds which will be aggregated to construct a product of weight

²We use shorthand notation for matrix concatenation such that $[W_{c,d,l}]_{c=1}^{C_l} \triangleq [W_{1,d,l}, W_{2,d,l}, \dots, W_{C_l,d,l}]$.

³We ignore the bias terms in the notation for simplicity.

⁴In this work, we consider Riemannian manifolds of normalized weights defined in the previous section. Formal definitions are given in the supp. mat.

manifolds (POM). Each $\mathcal{M}_{l,l} \in \mathcal{G}_l^g$ is called a component manifold of a product of weight manifolds which is denoted by $\mathbb{M}_{g,l}$. A weight $\omega_{g,l} \in \mathbb{M}_{g,l}$ is obtained by concatenating weights belonging to $\mathcal{M}_{l,l}$, $\forall l \in \mathcal{I}_l^g$, using $\omega_{g,l} = (\omega_1, \omega_2, \dots, \omega_{|\mathcal{I}_l^g|})$, where $|\mathcal{I}_l^g|$ is the cardinality of \mathcal{I}_l^g . A \mathcal{G}_l is called a *collection of POMs*. ■

We propose three schemes called POMs for input channels (PI), for output channels (PO) and input/output channels (PIO) to construct index sets. Indices of the sets are selected randomly using a hypergeometric distribution without replacement at the initialization of a training step, and fixed in the rest of the training. Implementation details and experimental analyses are given in the supp. mat.

III. OPTIMIZATION USING FINE-GRAINED SGD IN DNNs

A. Optimization on POMs in DNNs: Challenges and Solutions

Employment of a vanilla SGD on POMs with assurance to convergence to local or global minima for training DNNs using back-propagation (BP) with collections of POMs is challenging. More precisely, we observe early divergence of SGD, and exploding and vanishing gradients in the experiments, due to the following theoretical properties of collections of POMs:

- Geometric properties of a POM $\mathbb{M}_{g,l}$ can be different from those of its component manifolds \mathbb{M}_l , even if the component manifolds are identical. For example, we observe locally varying curvatures when we construct POMs of unit spheres. Weight manifolds with more complicated geometric properties can be obtained using the proposed PIO strategy, especially by constructing collections of POMs of non-identical manifolds. Therefore, assumption on existence of compact weight subsets in POMs may fail due to locally varying metrics within a nonlinear component manifold and among different component manifolds ⁵.
- When we optimize weights using SGD in DNNs, we first obtain gradients computed for each weight $\omega_{g,l} \in \mathbb{M}_{g,l}$ at the l^{th} layer from the $(l+1)^{\text{st}}$ layer using BP. Then, each weight $\omega_{g,l}$ moves on $\mathbb{M}_{g,l}$ according to the gradient. However, curvatures and metrics of $\mathbb{M}_{g,l}$ can locally vary, and they may be different from those of component manifolds of $\mathbb{M}_{g,l}$ as explained above. This geometric drawback causes two critical problems. First, weights can be moved incorrectly if we move them using only gradients computed for each individual component of the weights, as popularly employed for the Euclidean linear weight spaces. Second, due to incorrect employment of gradients and movement of weights, probability of failure of the SGD cannot be bounded, and convergence cannot be achieved (see proofs of Theorem 2, Corollary 1 and Corollary 2 for details). In practice, this causes unbounded increase or decrease of values of gradients and weights.

In order to address these problems for training DNNs, we first analyze the relationship between geometric properties of POMs and those of their component manifolds in the next theorem.

Remark 1. (See Lemma 1 given in the supp. mat. for the complete proof of the following propositions) Our main theoretical results regarding geometric properties of POMs are summarized as follows:

- 1) A metric defined on a product weight manifold $\mathbb{M}_{g,l}$ can be computed by superposition (i.e. linear combination) of Riemannian metrics of its component manifolds.
- 2) Sectional curvature of a product weight manifold $\mathbb{M}_{g,l}$ is lower bounded by 0. ■

We use the first result (1) for *projection* of Euclidean gradients obtained using BP onto product weight manifolds. More precisely, we can compute *norms of gradients* at weights on a product weight manifold by linear superposition of those computed on its component manifolds in FG-SGD. Thereby, we can move a weight on a product weight manifold by (i) retraction of components of the weight on component manifolds of the product weight manifold, and (ii) concatenation of projected weight components in FG-SGD. Note also that some sectional curvatures vanish on a product weight manifold $\mathbb{M}_{g,l}$ by the second result (2). For instance, suppose that each component weight manifold $\mathcal{M}_{l,l}$ of $\mathbb{M}_{g,l}$ is a unit two-sphere \mathbb{S}^2 , $\forall l \in \mathcal{I}_{\mathcal{G}_l}$. Then, $\mathbb{M}_{g,l}$ has unit curvature along two-dimensional subspaces of its tangent spaces, called two-planes. However, $\mathbb{M}_{g,l}$ has zero curvature along all two-planes spanning exactly two distinct spheres.

⁵Formal definitions and additional details are given in the supp. mat. to improve readability of the main text.

In addition, weights can always move according to a non-negative bound on sectional curvature of compact product weight manifolds on its tangent spaces. Therefore, we do not need to worry about varying positive and negative curvatures observed at its different component manifolds. The second result also suggests that learning rates need to be computed adaptively by a function of *norms of gradients* and *bounds on sectional curvatures* at each layer of the DNN and at each epoch of FG-SGD for each weight ω on each product weight manifold $\mathbb{M}_{g,l}$. We employ these results to analyze convergence of FG-SGD and compute its adaptive step size in the following sections.

TABLE I: Comparison of generalization bounds. \mathcal{O} denotes big-O and $\tilde{\mathcal{O}}$ is soft-O. $\delta_{l,F}$, $\delta_{l,2}$, and $\delta_{l,2\rightarrow 1}$ denotes upper bounds of the Frobenius norm $\|\omega_l\|_F \leq \delta_{l,F}$, spectral norm $\|\omega_l\|_2 \leq \delta_{l,2}$ and the sum of the Euclidean norms for all rows $\|\omega_l\|_{2\rightarrow 1} \leq \delta_{l,2\rightarrow 1}$ ($\ell_{2\rightarrow 1}$) of weights ω_l at the l^{th} layer of an L layer DNN using N samples. Suppose that all layers have the same width ϖ , weights have the same length \mathcal{K} and the same stride \mathfrak{s} . Then, generalization bounds are obtained for DNNs using these fixed parameters by $\|\omega_l\|_2 = \frac{\mathcal{K}}{\mathfrak{s}}$, $\|\omega_l\|_F = \sqrt{\varpi}$ and $\|\omega_l\|_{2\rightarrow 1} = \varpi$. We compute a concatenated weight matrix $\omega_{g,l} = (\omega_{g,l}^1, \omega_{g,l}^2, \dots, \omega_{g,l}^{|\mathfrak{g}|})$ for the g^{th} weight group of size $|\mathfrak{g}|, g = 1, 2, \dots, G_l, \forall l$ using a weight grouping strategy. Then, we have upper bounds of norms by $\|\omega_{g,l}\|_F \leq \delta_{g,l,F} \leq 1$, $\|\omega_{g,l}\|_2 \leq \delta_{g,l,2} \leq 1$ and $\|\omega_{g,l}\|_{2\rightarrow 1} \leq \delta_{g,l,2\rightarrow 1} \leq 1, g = 1, 2, \dots, G_l$, which are defined in Table IV.

	DNNs (dynamic group scaling)
Neyshabur et al. [22]	$\mathcal{O}\left(\frac{2^L \prod_{l=1}^L \prod_{g=1}^{G_l} \delta_{g,l,F}}{\sqrt{N}}\right)$
Bartlett et al. [3]	$\tilde{\mathcal{O}}\left(\frac{\prod_{l=1}^L \prod_{g=1}^{G_l} \delta_{g,l,2}}{\sqrt{N}} \left(\sum_{l=1}^L \prod_{g=1}^{G_l} \left(\frac{\delta_{g,l,2\rightarrow 1}}{\delta_{g,l,2}}\right)^{\frac{2}{3}}\right)^{\frac{3}{2}}\right)$
Neyshabur et al. [8]	$\tilde{\mathcal{O}}\left(\frac{\prod_{l=1}^L \prod_{g=1}^{G_l} \delta_{g,l,2}}{\sqrt{N}} \sqrt{L^2 \varpi \sum_{l=1}^L \prod_{g=1}^{G_l} \frac{\delta_{g,l,F}^2}{\delta_{g,l,2}^2}}\right)$

TABLE II: Comparison of norms of weights belonging to different weight manifolds. Suppose that weights $\omega_{g,l}^i \in \mathbb{R}^{A_l \times B_l}$ belonging to the g^{th} group of size $|\mathfrak{g}|, g = 1, 2, \dots, G_l, \forall l$ have the same size $A_l \times B_l$ for simplicity, and $\sigma(\omega_{g,l}^i)$ denotes the top singular value of $\omega_{g,l}^i$. Let $\|\omega_{g,l}^i\|_F$, $\|\omega_{g,l}^i\|_2$, and $\|\omega_{g,l}^i\|_{2\rightarrow 1}$, denote respectively the Frobenius, spectral and $\ell_{2\rightarrow 1}$ norms of the weight $\omega_{g,l}^i$. Then, we have $\|\omega_{g,l}\|_F \geq \left(\prod_{i=1}^{|\mathfrak{g}|} \|\omega_{g,l}^i\|_F\right)^{1/|\mathfrak{g}|}$, $\|\omega_{g,l}\|_2 \geq \left(\prod_{i=1}^{|\mathfrak{g}|} \|\omega_{g,l}^i\|_2\right)^{1/|\mathfrak{g}|}$ and $\|\omega_{g,l}\|_{2\rightarrow 1} \geq \left(\prod_{i=1}^{|\mathfrak{g}|} \|\omega_{g,l}^i\|_{2\rightarrow 1}\right)^{1/|\mathfrak{g}|}$.

Norms	(i) Sphere	(ii) Stiefel	(iii) Oblique
$\ \omega_{g,l}^i\ _2$	$\sigma(\omega_{g,l}^i)$	1.0	$\sigma(\omega_{g,l}^i)$
$\ \omega_{g,l}^i\ _F$	1.0	$(B_l)^{1/2}$	$(B_l)^{1/2}$
$\ \omega_{g,l}^i\ _{2\rightarrow 1}$	1.0	$(B_l)^{1/4}$	$(B_l)^{1/4}$

IV. BOUNDING GENERALIZATION ERRORS USING FINE-GRAINED WEIGHTS

Mathematically, norms of concatenated weights $\omega_{g,l}, \forall g$, are lower bounded by products of norms of component weights $\omega_{g,l}^i, \forall i$. We compute norms of weights belonging to each different manifold in Table IV. Weights are rescaled dynamically at each t^{th} epoch of an optimization method proposed to train DNNs using $\mathfrak{R}_{i,l}^t = \frac{\gamma_{i,l}}{\lambda_{i,l}^t}$, where $\gamma_{i,l} > 0$ is a geometric scaling parameter and $\lambda_{i,l}^t$ is the standard deviation of features input to the i^{th} weight in the g^{th} group $\omega_{g,l}^i, \forall i, g$. The scaling parameter $\mathfrak{R}_{i,l}^t$ enables us to upper bound the norms of weights by 1 (see Table VI). Computation of upper bounds are given in Proposition 1 in the supplemental material. The proof strategy is summarized as follows:

Algorithm 1 Optimization using FG-SGD on products manifolds of fine-grained weights.

- 1: **Input:** T (number of iterations), S (training set),
 Θ (set of hyperparameters), \mathcal{L} (a loss function), $\mathcal{I}_g^l \subseteq \mathcal{I}_{\mathcal{G}_l}, \forall g, l$.
 - 2: **Initialization:** Construct a collection of products of weight manifolds \mathcal{G}_l , initialize re-scaling parameters \mathcal{R}_l^t and initialize weights $\omega_{g,l}^t \in \mathbb{M}_{g,l}$ with $\mathcal{I}_g^l \subseteq \mathcal{I}_{\mathcal{G}_l}, \forall m, l$.
 - 3: **for** each iteration $t = 1, 2, \dots, T$ **do**
 - 4: **for** each layer $l = 1, 2, \dots, L$ **do**
 - 5: $\text{grad}\mathcal{L}(\omega_{g,l}^t) := \Pi_{\omega_{g,l}^t}(\text{grad}_E \mathcal{L}(\omega_{g,l}^t), \Theta, \mathcal{R}_l^t), \forall \mathcal{G}_l$.
 - 6: $v_t := h(\text{grad}\mathcal{L}(\omega_{g,l}^t), r(t, \Theta)), \forall \mathcal{G}_l$.
 - 7: $\omega_{g,l}^{t+1} := \phi_{\omega_{g,l}^t}(v_t, \mathcal{R}_l^t), \forall \omega_{g,l}^t, \forall \mathcal{G}_l$.
 - 8: **end for**
 - 9: **end for**
 - 10: **Output:** A set of estimated weights $\{\omega_{g,l}^T\}_{l=1}^L, \forall g$.
-

• Let $\mathfrak{b}_{i,l}$ be multiplication of the number of input channels and the size of the receptive field of the unit that employs $\omega_{g,l}^i$, and $\hat{\mathfrak{b}}_{i,l}$ be multiplication of the dimension of output feature maps and the number of output channels used at the l^{th} layer, respectively. Then, geometric scaling $\gamma_{i,l}$ of the weight space of $\omega_{g,l}^i$ is computed by

$$\gamma_{i,l} = \sqrt{\frac{1}{\mathfrak{b}_{i,l} + \hat{\mathfrak{b}}_{i,l}}}. \quad (2)$$

• We can consider that standard deviation of features satisfy $\lambda_{i,l}^t \geq 1$ using two approaches. First, by employing the central limit theory for weighted summation of random variables of features, we can prove that $\lambda_{i,l}^t$ converges to 1 asymptotically, as popularly employed in the previous works. Second, we can assume that we apply batch normalization (BN) by setting the re-scaling parameter of the BN to 1. Thereby, we can obtain $\frac{1}{\lambda_{i,l}^t} \leq 1$. By definition, $\gamma_{i,l}^2 < B_l, \forall i, l$. In order to show that $\sigma(\omega_{g,l}^i) \leq (\gamma_{i,l})^{-1}, \forall i, l$, we apply the Bai-Yin law [23], [24]. Thereby, we conclude that norms of concatenated weights belonging to groups given in Table VI are upper bounded by 1, if the corresponding component weights given in Table IV are rescaled by $\mathfrak{R}_{i,l}^t, \forall i, l, t$ during training.

Note that scaling by $\mathfrak{R}_{i,l}^t$ computed using (2) is different from the scaling method suggested in [13] such that our proposed method assures tighter upper bound for norms of weights. Our method also generalizes the scaling method given in [25] in two ways. First, we use size of input receptive fields and output feature spaces which determine dimension of weight manifolds, as well as number of input and output dimensions which determine number of manifolds used in groups. Second, we perform scaling not just at initialization but also at each t^{th} epoch of the optimization method. Therefore, diversity of weights is controlled and we can obtain weights uniformly distributed on the corresponding manifolds whose geometric properties change dynamically at each epoch. Applying this property with the results given in [11], we can prove that NNs applying the proposed scaling have no spurious local minima⁶. In addition, our method generalizes the scaling method proposed in [17] for weight normalization by incorporating geometric properties of weight manifolds.

A. Optimization on POMs using FG-SGD in DNNs

An algorithmic description of our proposed fine-grained SGD (FG-SGD) is given in Algorithm 1. At the initialization of the FG-SGD, we identify the component weight manifolds $\mathcal{M}_{i,l}$ of each product weight

⁶We omit the formal theorem and the proof on this result in this work to focus on our main goal and novelty for optimization with multiple weight manifolds.

manifold $\mathbb{M}_{g,l}$ according to the constraints that will be applied on the weights $\omega_{\iota} \in \mathcal{M}_{\iota,l}$ for each g^{th} group at each l^{th} layer⁷. For $t = 1$, each manifold $\mathcal{M}_{\iota,l}$ is scaled by $\mathfrak{R}_{\iota,l}^{t=1}$ using $\lambda_{\iota,l}^{t=1} = 1, \forall \iota, l$. For $t > 1$, each $\mathcal{M}_{\iota,l}$ is re-scaled by $\mathfrak{R}_{\iota,l}^t \in \mathcal{R}_{\iota,l}^t$ computing empirical standard deviation $\lambda_{\iota,l}^t$ of features input to each weight of $\mathcal{M}_{\iota,l}$, and $\mathcal{R}_{\iota,l}^t$ is the set of all re-scaling parameters computed at the t^{th} epoch at each l^{th} layer. When we employ a FG-SGD on a product weight manifold $\mathbb{M}_{g,l}$ each weight $\omega_{g,l}^t \in \mathbb{M}_{g,l}$ is moved on $\mathbb{M}_{g,l}$ in the descent direction of gradient of loss at each t^{th} step of the FG-SGD by the following steps:

Line 5 (Projection of gradients on tangent spaces): The gradient $\text{grad}_E \mathcal{L}(\omega_{g,l}^t)$, obtained using back-propagation from the upper layer, is projected onto the tangent space $\mathcal{T}_{\omega_{g,l}^t} \mathbb{M}_{g,l} = \times_{\iota \in \mathcal{I}_g^l} \mathcal{T}_{\omega_{\iota,l}^t} \mathbb{M}_{\iota,l}$ to compute $\text{grad} \mathcal{L}(\omega_{g,l}^t)$ at the weight $\omega_{g,l}^t$ using the results given in Remark 1, where $\mathcal{T}_{\omega_{\iota,l}^t} \mathbb{M}_{\iota,l}$ is the tangent space at $\omega_{\iota,l}^t$ on the component manifold $\mathbb{M}_{\iota,l}$ of $\mathbb{M}_{g,l}$.

Line 6 (Movement of weights on tangent spaces): The weight $\omega_{g,l}^t$ is moved on $\mathcal{T}_{\omega_{g,l}^t} \mathbb{M}_{g,l}$ using

$$h(\text{grad} \mathcal{L}(\omega_{g,l}^t), r(t, \Theta)) = -\frac{r(t, \Theta)}{\zeta(\omega_{g,l}^t)} \text{grad} \mathcal{L}(\omega_{g,l}^t), \quad (3)$$

where $r(t, \Theta)$ is the learning rate that satisfies

$$\sum_{t=0}^{\infty} r(t, \Theta) = +\infty \text{ and } \sum_{t=0}^{\infty} r(t, \Theta)^2 < \infty, \quad (4)$$

$$\zeta(\omega_{G^m}^t) = \max\{1, \Gamma_1^t\}^{\frac{1}{2}} \quad (5)$$

$\Gamma_1^t = (R_{g,l}^t)^2 \Gamma_2^t$, $R_{g,l}^t \triangleq \|\text{grad} \mathcal{L}(\omega_{g,l}^t)\|_2$ is computed using (17), $\Gamma_2^t = \max\{(2\rho_{g,l}^t + R_{g,l}^t)^2, (1 + \mathbf{c}_{g,l}(\rho_{g,l}^t + R_{g,l}^t))\}$, $\mathbf{c}_{g,l}$ is the sectional curvature of $\mathbb{M}_{g,l}$, $\rho_{g,l}^t \triangleq \rho(\omega_{g,l}^t, \hat{\omega}_{g,l})$ is the geodesic distance between $\omega_{g,l}^t$ and a local minima $\hat{\omega}_{g,l}$ on $\mathbb{M}_{g,l}$.

The following result is used for computation of the ℓ_2 norm of gradients.

Theorem 1 (Computation of gradients on tangent spaces). The ℓ_2 norm $\|\text{grad} \mathcal{L}(\omega_{g,l}^t)\|_2$ of the gradient $\text{grad} \mathcal{L}(\omega_{g,l}^t)$ residing on $\mathcal{T}_{\omega_{g,l}^t} \mathbb{M}_{g,l}$ at the t^{th} epoch and the l^{th} layer can be computed by

$$\|\text{grad} \mathcal{L}(\omega_{g,l}^t)\|_2 = \left(\sum_{\iota \in \mathcal{I}_g^l} \text{grad} \mathcal{L}(\omega_{\iota,l}^t)^2 \right)^{\frac{1}{2}}, \quad (6)$$

where $\text{grad} \mathcal{L}(\omega_{\iota,l}^t)$ is the gradient computed for $\omega_{\iota,l}^t$ on the tangent space $\mathcal{T}_{\omega_{\iota,l}^t} \mathbb{M}_{\iota,l}$, $\forall \iota \in \mathcal{I}_g^l$. ■

Line 7 (Projection of moved weights onto product of manifolds): The moved weight located at v_t is projected onto $\mathbb{M}_{g,l}$ re-scaled by $\mathcal{R}_{\iota,l}^t$ using $\phi_{\omega_{g,l}^t}(v_t, \mathcal{R}_{\iota,l}^t)$ to compute $\omega_{g,l}^{t+1}$, where $\phi_{\omega_{g,l}^t}(v_t, \mathcal{R}_{\iota,l}^t)$ is an exponential map, or a retraction, i.e. an approximation of the exponential map [26]. The function $\zeta(\omega_{g,l}^t)$ used for computing step size in (30) is employed as a regularizer to control the change of gradient $\text{grad} \mathcal{L}(\omega_{g,l}^t)$ at each step of FG-SGD. This property is examined in the experimental analyses in the supp. mat. For computation of $\zeta(\omega_{g,l}^t)$, we use (17) with Theorem 1. In FG-SGD, weights residing on each POM are moved and projected jointly on the POMs, by which we can employ their interaction using the corresponding gradients considering nonlinear geometry of manifolds unlike SGD methods studied in the literature. G-SGD can consider interactions between component manifolds as well as those between POMs in groups of weights. Employment of (30) and (4) at line 7, and retractions at line 8 are essential for assurance of convergence as explained next.

⁷In the experimental analyses, we use the oblique and the Stiefel manifolds as well as the sphere and the Euclidean space to identify component manifolds $\mathcal{M}_{\iota,l}$. Details are given in the supplemental material.

TABLE III: Mean \pm standard deviation of classification error (%) are given for results obtained using Resnet-50/101, SENet-Resnet-50/101, and 110-layer Resnets with constant depth (RCD) on Imagenet.

Model	Imagenet(Resnet-50)	Imagenet(SENet-Resnet-50)
Euc.	24.73 \pm 0.32	23.31 \pm 0.55
St	23.77 \pm 0.27	23.09 \pm 0.41
POMs of St	23.61 \pm 0.22	22.97 \pm 0.29
PIO (Sp+Ob+St)	23.04 \pm 0.10	22.67 \pm 0.15
PIO (Sp+Ob+St+Euc.)	22.89 \pm 0.08	22.53 \pm 0.11
(Additional results)	Imagenet(Resnet-101)	Imagenet(SENet-Resnet-101)
Euc.	23.15 \pm 0.09	22.38 \pm 0.30
PIO (Sp+Ob+St)	22.83 \pm 0.06	21.93 \pm 0.12
PIO (Sp+Ob+St+Euc.)	22.75 \pm 0.02	21.76 \pm 0.09

B. Convergence Properties of FG-SGD

Convergence properties of the proposed FG-SGD used to train DNNs are summarized as follows:

Convergence to local minima: The loss function of a non-linear DNN, which employs the proposed FG-SGD, converges to a local minimum, and the corresponding gradient converges to zero almost surely (a.s.). The formal theorem and proof are given in Theorem 2 in the supplemental material.

Convergence to global minima: Loss functions of particular DNNs such as linear DNNs, one-hidden-layer CNNs, one-hidden-layer Leaky Relu networks, nonlinear DNNs with specific network structures (e.g. pyramidal networks), trained using FG-SGD, converge to a global minimum a.s. under mild assumptions on data (e.g. being distributed from Gaussian distribution, normalized, and realized by DNNs). The formal theorem and proof of this result are given in Corollary 1 in the supp. mat. The proof idea is to use the property that local minima of loss functions of these networks are global minima under these assumptions, by employing the results given in the recent works [27], [28], [29], [30], [31], [32], [33], [34], [35], [36].

An example for adaptive computation of step size: Suppose that \mathbb{M}_l are identified by $n_l \geq 2$ dimensional unit sphere, or the sphere scaled by the proposed scaling method. If step size is computed using (30) with

$$\tau(\omega_{G_l^m}^t) = (\max\{1, (R_{G_l^m}^t)^2(2 + R_{G_l^m}^t)^2\})^{\frac{1}{2}}, \quad (7)$$

then the loss function converges to local minima for a generic class of nonlinear DNNs, and to global minima for DNNs characterized in Corollary 1. The formal theorem and proof of this result are given in Corollary 2 in the supp. mat.

We consider analyzing global convergence properties of FG-SGD using different manifolds for larger class of nonlinear DNNs relaxing these assumptions and conditions as a future work.

V. EXPERIMENTAL ANALYSES

We examine the proposed FG-SGD method for training DNNs using different architectures with different configurations on benchmark datasets for image classification tasks. We provide representative results in Table XV in this main text, and the other results in the supp. mat. Implementation details and analysis of computational complexity of the proposed methods are given in the supplemental material. We give accuracy of DNNs for baseline Euclidean (Euc.), the sphere (Sp), the oblique (Ob) and the Stiefel (St) manifold in Table XV. POMs of St denotes results for weights employed on all input and output channels residing on a POM of St. PIO (*manifolds*) denotes results for collections of POMs of *manifolds* using PIO.

Table XV shows results using the state-of-the-art Squeeze-and-Excitation (SE) blocks [37] implemented for Resnets with 50 layers (Resnet-50) on Imagenet. We run the experiments 3 times and provide the average performance. We first observe that PIO boosts the performance of baseline Euc. (24.73%) by 1.84% if sets of weights are employed using Euc, Sp, Ob and St (22.89%). We note that the sets computed for Resnet-50 outperform Resnets with 101 layers (23.15) by 0.26%. SE blocks aim to aggregate channel-wise descriptive statistics (i.e. mean of convolution outputs) of local descriptors of images to feature maps for

each channel. In FG-SGD, we use standard deviation (std) of features extracted from each batch and size of receptive fields of units while defining and updating weight manifolds (see Section 3.3 in supp. mat.). Unlike SE blocks, FG-SGD computes statistical and geometric properties for different sets of input and output channels, and used to update weights by FG-SGD. This property helps FG-SGD to further boost the performance. For instance, we observe that collections of manifolds (23.04% and 22.89% error) outperform SENet-Resnet-50 (23.31% error). Although FG-SGD estimates standard deviation using moving averages as utilized in batch normalization [38], SE blocks estimates the statistics using small networks. Therefore, we conjecture that they provide complementary descriptive statistics (mean and std). The experimental results justify this claim such that sets implemented in SENet-Resnet-50 further boost the performance by providing 22.53% error.

VI. CONCLUSION AND DISCUSSION

We introduced and elucidated a problem of training CNNs using multiple constraints employed on convolution weights with convergence properties. Following our theoretical results, we proposed the FG-SGD algorithm and adaptive step size estimation methods for optimization on collections of POMs that are identified by the constraints. The experimental results show that our proposed methods can improve convergence properties and classification performance of CNNs. Overall, the results show that employment of collections of POMs using FG-SGD can boost the performance of various different CNNs on benchmark datasets. We consider a research direction for investigating how far local minima are from global minima in search spaces of FG-SGD using products of weight manifolds with nonlinear DNNs and their convergence rates. We believe that our proposed framework will be useful and inspiring for researchers to study geometric properties of parameter spaces of deep networks, and to improve our understanding of deep feature representations.

SUPPLEMENTAL MATERIAL

APPENDIX A

BOUNDING GENERALIZATION ERRORS USING FINE-GRAINED WEIGHTS

Proposition 1 (Bounding norms of weight matrices and generalization errors of DNNs). Suppose that DNNs given in Table VI are trained using weights renormalized by the renormalization method proposed in the main text according to the Frobenius, spectral and column/row wise norms with reparameterization parameters $\mathfrak{R}_{i,l}^t, \forall i, l, t$ with $\lambda_{i,l}^t \geq 1$. Then, norms of renormalized weight matrices are upper bounded by a constant number, and generalization errors of the corresponding DNNs are asymptotically bounded as given in the rightmost column of the Table VI, denoted by **DNNs** (our proposed reparameterization).

Proof. Suppose that matrices of weights $\omega_{g,l}^i \in \mathbb{R}^{A_l \times B_l}$ belonging to the g^{th} group of size $|g|, g = 1, 2, \dots, G_l, \forall l$ have the same size $A_l \times B_l$ for simplicity, and $\sigma(\omega_{g,l}^i)$ denotes the top singular value of $\omega_{g,l}^i$. Let $\|\omega_{g,l}^i\|_F, \|\omega_{g,l}^i\|_2,$ and $\|\omega_{g,l}^i\|_{2 \rightarrow 1}$, denote respectively the Frobenius, spectral and $\ell_{2 \rightarrow 1}$ norms of the weight $\omega_{g,l}^i$. We note that, matrices of weights $\omega_{g,l}^i$ belonging to the g^{th} group are concatenated by $\omega_{g,l} = (\omega_{g,l}^1, \omega_{g,l}^2, \dots, \omega_{g,l}^g), \forall g = 1, 2, \dots, G_l$, to perform group-wise operations in DNNs. Thereby, we can employ bounds for norms of each concatenated matrix in generalization error bounds given in the leftmost column of Table VI, denoted by **DNNs** (bounds on norms), and obtain the bounds given in the rightmost column of the Table VI, denoted by **DNNs**(our proposed reparameterization).

We compute norms of matrices of normalized weights $\omega_{g,l}^i$ belonging to each different manifold in Table IV. These norms are computed using simple matrix calculus considering definitions of matrices residing on each manifold according to the definition given in Table V. From these calculations given in Table IV, we observe that, the maximum of norm values that a weight $\omega_{g,l}^i$ belonging to the sphere can achieve is $\mathbb{M}_{sp}(\omega_{g,l}^i) = \sigma(\omega_{g,l}^i)$, that of a weight belonging to the Stiefel manifold is $\mathbb{M}_{st}(\omega_{g,l}^i) = (B_l)^{1/2}$, and that of a weight belonging to the oblique manifold is $\mathbb{M}_{ob}(\omega_{g,l}^i) = \max\{(B_l)^{1/2}, \sigma(\omega_{g,l}^i)\}$.

In our proposed renormalization method, we first normalize each weight matrix such that the norm of the matrix $\omega_{g,l}^i$ can have one of these values $\mathbb{M}_{sp}(\omega_{g,l}^i)$, $\mathbb{M}_{st}(\omega_{g,l}^i)$ and $\mathbb{M}_{ob}(\omega_{g,l}^i)$. Therefore, we need to reparameterize weight matrices such that norm of each reparameterized weight is less than 1.0. For this purpose, we need show that the rescaling of these norm values by $\mathfrak{R}_{i,l}^t$ is upper bounded by 1.0.

Weights are rescaled dynamically at each t^{th} epoch of an optimization method proposed to train DNNs using $\mathfrak{R}_{i,l}^t = \frac{\gamma_{i,l}}{\lambda_{i,l}^t}$, where $0 < \gamma_{i,l} < 1.0$ is a geometric scaling parameter and $\lambda_{i,l}^t$ is the standard deviation of features input to the i^{th} weight in the g^{th} group $\omega_{g,l}^i$, $\forall i, g$. By assumption, $\lambda_{i,l}^t \leq 1.0$, $\forall i, t, l$. By definition, $B_l \gamma_{i,l}^2 \leq 1.0$, $\forall i, l$. In order to show that $\sigma(\omega_{g,l}^i) \leq (\gamma_{i,l})^{-1}$, $\forall i, l$, we apply the Bai-Yin law [23], [24]. Thereby, we conclude that norms of concatenated weights belonging to groups given in Table VI are upper bounded by 1, if the corresponding component weights given in Table IV are rescaled by $\mathfrak{R}_{i,l}^t$, $\forall i, l, t$ during training of DNNs.

Since norm of each weight matrix $\omega_{g,l}^i$ is bounded by 1.0, their multiplication for all $g = 1, 2, \dots, G_l$ and $\forall l$ is also bounded by 1.0. □

TABLE IV: Comparison of norms of weights belonging to different weight manifolds.

Norms	(i) Sphere	(ii) Stiefel	(iii) Oblique
$\ \omega_{g,l}^i\ _2$	$\sigma(\omega_{g,l}^i)$	1.0	$\sigma(\omega_{g,l}^i)$
$\ \omega_{g,l}^i\ _F$	1.0	$(B_l)^{1/2}$	$(B_l)^{1/2}$
$\ \omega_{g,l}^i\ _{2 \rightarrow 1}$	1.0	$(B_l)^{1/4}$	$(B_l)^{1/4}$

TABLE V: Embedded weight manifolds \mathcal{M}_l used for construction of collection of POMs \mathbb{M}_{G_l} , $\forall l$, in the experimental analyses. The Frobenius norm of a convolution weight ω is denoted by $\|\omega\|_F$. The b^{th} column vector of a weight matrix $\omega \in \mathbb{R}^{A_l \times B_l}$ is denoted by ω_b . An $B_l \times B_l$ identity matrix is denoted by I_{B_l} .

Manifolds	Definitions
The Sphere	$\mathcal{S}(A_l, B_l) = \{\omega \in \mathbb{R}^{A_l \times B_l} : \ \omega\ _F = 1\}$
The Oblique	$\mathcal{OB}(A_l, B_l) = \{\omega \in \mathbb{R}^{A_l \times B_l} : \ \omega_b\ _F = 1, \forall b = 1, 2, \dots, B_l\}$
The Stiefel	$\mathcal{St}(A_l, B_l) = \{\omega \in \mathbb{R}^{A_l \times B_l} : (\omega^T \omega) = I_{B_l}\}$

APPENDIX B

PROOFS OF THEOREMS GIVEN IN THE MAIN TEXT

Definition 2 (Sectional curvature of component manifolds). Let $\mathfrak{X}(\mathcal{M}_{l,l})$ denote the set of smooth vector fields on $\mathcal{M}_{l,l}$. The sectional curvature of $\mathcal{M}_{l,l}$ associated with a two dimensional subspace $\mathfrak{T} \subset \mathcal{T}_{\omega_l} \mathcal{M}_{l,l}$ is defined by

$$\mathfrak{c}_l = \frac{\langle \mathcal{C}_l(X_{\omega_l}, Y_{\omega_l})Y_{\omega_l}, X_{\omega_l} \rangle}{\langle X_{\omega_l}, X_{\omega_l} \rangle \langle Y_{\omega_l}, Y_{\omega_l} \rangle - \langle X_{\omega_l}, Y_{\omega_l} \rangle^2} \quad (8)$$

where $\mathcal{C}_l(X_{\omega_l}, Y_{\omega_l})Y_{\omega_l}$ is the Riemannian curvature tensor, $\langle \cdot, \cdot \rangle$ is an inner product, $X_{\omega_l} \in \mathfrak{X}(\mathcal{M}_{l,l})$ and $Y_{\omega_l} \in \mathfrak{X}(\mathcal{M}_{l,l})$ form a basis of \mathfrak{T} . ■

TABLE VI: Comparison of generalization bounds. \mathcal{O} denotes big-O and $\tilde{\mathcal{O}}$ is soft-O. $\delta_{l,F}$, $\delta_{l,2}$, and $\delta_{l,2 \rightarrow 1}$ denotes upper bounds of the Frobenius norm $\|\omega_l\|_F \leq \delta_{l,F}$, spectral norm $\|\omega_l\|_2 \leq \delta_{l,2}$ and the sum of the Euclidean norms for all rows $\|\omega_l\|_{2 \rightarrow 1} \leq \delta_{l,2 \rightarrow 1}$ ($\ell_{2 \rightarrow 1}$) of weights ω_l at the l^{th} layer of an L layer DNN using N samples. Suppose that all layers have the same width ϖ , weights have the same length \mathcal{K} and the same stride \mathfrak{s} . Then, generalization bounds are obtained for DNNs using these fixed parameters by $\|\omega_l\|_2 = \frac{\mathcal{K}}{\mathfrak{s}}$, $\|\omega_l\|_F = \sqrt{\varpi}$ and $\|\omega_l\|_{2 \rightarrow 1} = \varpi$. We compute a concatenated weight matrix $\omega_{g,l} = (\omega_{g,l}^1, \omega_{g,l}^2, \dots, \omega_{g,l}^{|\mathfrak{g}|})$ for the g^{th} weight group of size $|\mathfrak{g}|$, $g = 1, 2, \dots, G_l, \forall l$ using a weight grouping strategy. Then, we have upper bounds of norms by $\|\omega_{g,l}\|_F \leq \delta_{g,l,F} \leq 1$, $\|\omega_{g,l}\|_2 \leq \delta_{g,l,2} \leq 1$ and $\|\omega_{g,l}\|_{2 \rightarrow 1} \leq \delta_{g,l,2 \rightarrow 1} \leq 1, g = 1, 2, \dots, G_l$, which are defined in Table IV.

	DNNs (dynamic group scaling)
Neysshabur et al. [22]	$\mathcal{O}\left(\frac{2^L \prod_{l=1}^L \prod_{g=1}^{G_l} \delta_{g,l,F}}{\sqrt{N}}\right)$
Bartlett et al. [3]	$\tilde{\mathcal{O}}\left(\frac{\prod_{l=1}^L \prod_{g=1}^{G_l} \delta_{g,l,2}}{\sqrt{N}} \left(\sum_{l=1}^L \prod_{g=1}^{G_l} \left(\frac{\delta_{g,l,2 \rightarrow 1}}{\delta_{g,l,2}}\right)^{\frac{2}{3}}\right)^{\frac{3}{2}}\right)$
Neysshabur et al. [8]	$\tilde{\mathcal{O}}\left(\frac{\prod_{l=1}^L \prod_{g=1}^{G_l} \delta_{g,l,2}}{\sqrt{N}} \sqrt{L^2 \varpi \sum_{l=1}^L \prod_{g=1}^{G_l} \frac{\delta_{g,l,F}^2}{\delta_{g,l,2}^2}}\right)$

Definition 3 (Riemannian connection on component embedded weight manifolds). Let $\mathfrak{X}(\mathcal{M}_{l,l})$ denote the set of smooth vector fields on $\mathcal{M}_{l,l}$ and $\mathfrak{F}(\mathcal{M}_{l,l})$ denote the set of smooth scalar fields on $\mathcal{M}_{l,l}$. The Riemannian connection $\bar{\nabla}$ on $\mathcal{M}_{l,l}$ is a mapping [26]

$$\bar{\nabla} : \mathfrak{X}(\mathcal{M}_{l,l}) \times \mathfrak{X}(\mathcal{M}_{l,l}) \rightarrow \mathfrak{X}(\mathcal{M}_{l,l}) : (X_{\omega_l}, Y_{\omega_l}) \mapsto \bar{\nabla} X_{\omega_l} Y_{\omega_l} \quad (9)$$

which satisfies the following properties:

- 1) $\bar{\nabla}_p X_{\omega_l} + q Y_{\omega_l} Z_{\omega_l} = p \bar{\nabla} Z_{\omega_l} + q \nabla_{Y_{\omega_l}} Z_{\omega_l}$,
- 2) $\bar{\nabla} X_{\omega_l} (\alpha Y_{\omega_l} + \beta Z_{\omega_l}) = \alpha \bar{\nabla}_{X_{\omega_l}} Y_{\omega_l} + \beta \bar{\nabla}_{X_{\omega_l}} Z_{\omega_l}$,
- 3) $\bar{\nabla}_{X_{\omega_l}} (p Y_{\omega_l}) = (X_{\omega_l} p) Y_{\omega_l} + p \bar{\nabla}_{X_{\omega_l}} Y_{\omega_l}$,
- 4) $\bar{\nabla}_{X_{\omega_l}} Y_{\omega_l} - \bar{\nabla}_{Y_{\omega_l}} X_{\omega_l} = [X_{\omega_l}, Y_{\omega_l}]$ and
- 5) $Z_{\omega_l} \langle X_{\omega_l}, Y_{\omega_l} \rangle = \langle \bar{\nabla}_{Z_{\omega_l}} X_{\omega_l}, Y_{\omega_l} \rangle + \langle X_{\omega_l}, \bar{\nabla}_{Z_{\omega_l}} Y_{\omega_l} \rangle$

where $X_{\omega_l}, Y_{\omega_l}, Z_{\omega_l} \in \mathfrak{X}(\mathcal{M}_{l,l})$, $p, q \in \mathfrak{F}(\mathcal{M}_{l,l})$, $\alpha, \beta \in \mathbb{R}$, $\langle \cdot, \cdot \rangle$ is an inner product, $[X_{\omega_l}, Y_{\omega_l}]$ is the Lie bracket of X_{ω_l} and Y_{ω_l} , and defined by $[X_{\omega_l}, Y_{\omega_l}]p = X_{\omega_l}(Y_{\omega_l}p) - Y_{\omega_l}(X_{\omega_l}p)$, $\forall p \in \mathfrak{F}(\mathcal{M}_{l,l})$.

Lemma 1 (Metric and curvature properties of POMs). Suppose that $u_l \in \mathcal{T}_{\omega_l} \mathcal{M}_l$ and $v_l \in \mathcal{T}_{\omega_l} \mathcal{M}_l$ are tangent vectors belonging to the tangent space $\mathcal{T}_{\omega_l} \mathcal{M}_l$ computed at $\omega_l \in \mathcal{M}_l$, $\forall l \in \mathcal{I}_{G_l}$. Then, tangent vectors $u_{G_l} \in \mathcal{T}_{\omega_{G_l}} \mathbb{M}_{G_l}$ and $v_{G_l} \in \mathcal{T}_{\omega_{G_l}} \mathbb{M}_{G_l}$ are computed at $\omega_{G_l} \in \mathbb{M}_{G_l}$ by concatenation as $u_{G_l} = (u_1, u_2, \dots, u_{|\mathcal{I}_{G_l}|})$ and $v_{G_l} = (v_1, v_2, \dots, v_{|\mathcal{I}_{G_l}|})$. If each weight manifold \mathcal{M}_l is endowed with a Riemannian metric \mathfrak{d}_l , then a G_l -POM is endowed with the metric \mathfrak{d}_{G_l} computed by

$$\mathfrak{d}_{G_l}(u_{G_l}, v_{G_l}) = \sum_{l \in \mathcal{I}_{G_l}} \mathfrak{d}_l(u_l, v_l). \quad (10)$$

In addition, suppose that \bar{C}_l is the Riemannian curvature tensor field (endomorphism) [39] of \mathcal{M}_l , $x_l, y_l \in \mathcal{T}_{\omega_l} \mathcal{M}_l$, $\forall l \in \mathcal{I}_{G_l}$ defined by

$$\bar{C}_l(u_l, v_l, x_l, y_l) = \langle C_l(U, V)X, Y \rangle_{\omega_l}, \quad (11)$$

where U, V, X, Y are vector fields such that $U_{\omega_l} = u_l$, $V_{\omega_l} = v_l$, $X_{\omega_l} = x_l$, and $Y_{\omega_l} = y_l$. Then, the Riemannian curvature tensor field \bar{C}_{G_l} of \mathbb{M}_{G_l} is computed by

$$\bar{C}_{G_l}(u_{G_l}, v_{G_l}, x_{G_l}, y_{G_l}) = \sum_{l \in \mathcal{I}_{G_l}} \bar{C}_l(u_l, v_l, x_l, y_l), \quad (12)$$

where $x_{G_l} = (x_1, x_2, \dots, x_{|\mathcal{I}_{G_l}|})$ and $y_{G_l} = (y_1, y_2, \dots, y_{|\mathcal{I}_{G_l}|})$. Moreover, \mathbb{M}_{G_l} has never strictly positive sectional curvature \mathfrak{c}_{G_l} in the metric (10). In addition, if \mathbb{M}_{G_l} is compact, then \mathbb{M}_{G_l} does not admit a metric with negative sectional curvature \mathfrak{c}_{G_l} . ■

Proof. Since each weight manifold $\mathcal{M}_{\bar{l},l}$ is a Riemannian manifold, \mathfrak{d}_l is a Riemannian metric such that $\mathfrak{d}_l(u_l, v_l) = \langle u_l, v_l \rangle$. Thereby,

$$\mathfrak{d}_{G_l}(u_{G_l}, v_{G_l}) = \langle u_{G_l}, v_{G_l} \rangle = \sum_{\iota \in \mathcal{I}_{G_l}} \langle u_\iota, v_\iota \rangle \sum_{\iota \in \mathcal{I}_{G_l}} \mathfrak{d}_l(u_\iota, v_\iota) \quad (13)$$

and we obtain (10). In order to derive (12), we first compute

$$\left\langle \sum_{\iota \in \mathcal{I}_{G_l}} u_\iota, \sum_{\iota \in \mathcal{I}_{G_l}} v_\iota \right\rangle = \sum_{\iota \in \mathcal{I}_{G_l}} \langle u_\iota, v_\iota \rangle. \quad (14)$$

Then, we use the equations for the Lie bracket by

$$\left[\sum_{\iota \in \mathcal{I}_{G_l}} u_\iota, \sum_{\iota \in \mathcal{I}_{G_l}} v_\iota \right] = \sum_{\iota \in \mathcal{I}_{G_l}} [u_\iota, v_\iota]. \quad (15)$$

Next, we employ the Koszul's formula [39] by

$$2 \langle \bar{\nabla}_{u_l} v_l, x_l \rangle = u_l \langle v_l, x_l \rangle + v_l \langle x_l, u_l \rangle - x_l \langle u_l, v_l \rangle + \langle x_l, [u_l, v_l] \rangle - \langle v_l, [u_l, x_l] \rangle - \langle u_l, [v_l, x_l] \rangle$$

such that

$$\bar{\nabla}_{\bar{u}}(\bar{v}) = \sum_{\iota \in \mathcal{I}_{G_l}} \bar{\nabla}_{u_\iota}(v_\iota), \quad (16)$$

where $\bar{u} = \sum_{\iota \in \mathcal{I}_{G_l}} u_\iota$ and $\bar{v} = \sum_{\iota \in \mathcal{I}_{G_l}} v_\iota$. Using (11) and definition of the curvature with (13), (14), (15), and (16), we obtain (12).

In order to show that \mathbb{M}_{G_l} has never strictly positive sectional curvature \mathfrak{c}_{G_l} in the metric (10), it is sufficient to show that some sectional curvatures always vanish. Suppose that U is a vector field on \mathbb{M}_{G_l} along a component weight manifold $\mathcal{M}_{\bar{l},l}$ such that no local coordinate o of $\mathcal{M}_{\bar{l}}$ and $\frac{\partial}{\partial o}$ are present in local coordinates of U , $\forall \iota \neq \bar{l}$, $\bar{l} \in \mathcal{I}_{G_l}$. In addition, suppose that \bar{U} is a vector field along $\mathcal{M}_{\bar{l}}$. Then, $\bar{\nabla}_U \bar{U} = 0$, $\forall \iota, \bar{l} \in \mathcal{I}_{G_l}$. By employing (16), we have $\bar{C}_l(u_l, v_l, x_l, y_l) = 0$. Then, we use (12) to obtain $\bar{C}_{G_l}(u_{G_l}, v_{G_l}, x_{G_l}, y_{G_l}) = 0$. Therefore, following the definition of the sectional curvature, for arbitrary vector fields on component manifolds, \mathbb{M}_{G_l} has never strictly positive sectional curvature \mathfrak{c}_{G_l} in the metric (10). Since \mathbb{M}_{G_l} is a Riemannian manifold, if \mathbb{M}_{G_l} is compact, then \mathbb{M}_{G_l} does not admit a metric with negative sectional curvature \mathfrak{c}_{G_l} by the Preissmann's theorem [40]⁸. □

Theorem 1 (Computation of gradients on tangent spaces). The ℓ_2 norm $\|\text{grad}\mathcal{L}(\omega_{G_l^m}^t)\|_2$ of the gradient $\text{grad}\mathcal{L}(\omega_{G_l^m}^t)$ residing on $\mathcal{T}_{\omega_{G_l^m}^t} \mathbb{M}_{G_l^m}$ at the t^{th} epoch and the l^{th} layer can be computed by

$$\|\text{grad}\mathcal{L}(\omega_{G_l^m}^t)\|_2 = \left(\sum_{\iota \in \mathcal{I}_{G_l^m}} \text{grad}\mathcal{L}(\omega_{l,\iota}^t)^2 \right)^{\frac{1}{2}}, \quad (17)$$

where $\text{grad}\mathcal{L}(\omega_{l,\iota}^t)$ is the gradient computed for the weight $\omega_{l,\iota}^t$ on the tangent space $\mathcal{T}_{\omega_{l,\iota}^t} \mathbb{M}_l$, $\forall \iota \in \mathcal{I}_{G_l^m}$. ■

Proof. We use the inner product for the Riemannian metric $\mathfrak{d}_{G_l}(\text{grad}\mathcal{L}(\omega_{G_l^m}^t), \text{grad}\mathcal{L}(\omega_{G_l^m}^t))$ and

$\mathfrak{d}_l(\text{grad}\mathcal{L}(\omega_{l,\iota}^t), \text{grad}\mathcal{L}(\omega_{l,\iota}^t))$ of manifolds $\mathbb{M}_{G_l^m}$ and \mathbb{M}_l , $\forall \iota$, respectively. By definition of the product manifold, we have

$$\text{grad}\mathcal{L}(\omega_{G_l^m}^t) = \left(\text{grad}\mathcal{L}(\omega_{l,1}^t), \text{grad}\mathcal{L}(\omega_{l,2}^t), \text{grad}\mathcal{L}(\omega_{l,|\mathcal{I}_{G_l}|}^t) \right). \quad (18)$$

⁸see Theorem 24 in [40].

Thereby, we can apply bilinearity of inner product in Lemma 1 and obtain

$$\|\text{grad}\mathcal{L}(\omega_{G_l^m}^t)\|_2^2 = \left(\sum_{l \in \mathcal{I}_{G_l^m}} \text{grad}\mathcal{L}(\omega_{l,\iota}^t)^2 \right), \quad (19)$$

where $\|\cdot\|_2^2$ is the squared l_2 norm. The result follows by applying the square root to (19). \square

Theorem 2 (Convergence of the FG-SGD). Suppose that there exists a local minimum $\hat{\omega}_{G_l} \in \mathbb{M}_{G_l}, \forall G_l \subseteq \mathcal{G}_l, \forall l$, and $\exists \epsilon > 0$ such that $\inf_{\rho_{G_l}^t > \epsilon^{\frac{1}{2}}} \left\langle \phi_{\omega_{G_l}^t} (\hat{\omega}_{G_l})^{-1}, \nabla \mathcal{L}(\omega_{G_l}^t) \right\rangle < 0$, where ϕ is an exponential map or a twice continuously differentiable retraction, and $\langle \cdot, \cdot \rangle$ is the inner product. Then, the loss function and the gradient converges almost surely (a.s.) by $\mathcal{L}(\omega_{G_l}^t) \xrightarrow[t \rightarrow \infty]{\text{a.s.}} \mathcal{L}(\hat{\omega}_{G_l})$, and $\nabla \mathcal{L}(\omega_{G_l}^t) \xrightarrow[t \rightarrow \infty]{\text{a.s.}} 0$, for each $\mathbb{M}_{G_l}, \forall l$. \blacksquare

Proof. In this theorem, we generalize the proof idea of Theorem 4.1 and 4.2 given in [13], and Theorem 3 given in [41] for collections of products of embedded weight manifolds (POMs) for training of CNNs. The proof idea is to show that $\rho_{G_l}^t \triangleq \rho(\omega_{l,\iota}^t, \hat{\omega}_{l,\iota})$ converges almost surely to 0 as $t \rightarrow \infty$. For this purpose, we need to first model the change of gradient on the geodesic $\rho_{G_l}^t$ by defining a function $\Psi_t \triangleq \psi((\rho_{G_l}^t)^2)$ according to the following constraints [41];

- $\Psi_t = 0$, for $0 \leq \rho_{G_l}^t \leq \sqrt{\epsilon}$.
- $0 < \Psi_t'' \leq 2$, for $\sqrt{\epsilon} \leq \rho_{G_l}^t \leq \sqrt{\epsilon + 1}$.
- $\Psi_t' = 1$, for $\rho_{G_l}^t \geq \sqrt{\epsilon + 1}$.

Then, we compute gradients and geodesics on collections of POMs using (10) given in Lemma 1 by

$$\|\text{grad}\mathcal{L}(\omega_{G_l}^t)\|_2 = \left(\sum_{\omega_{l,\iota}^t \in \mathbb{M}_{l,\iota} \in \mathcal{I}_{G_l}} \text{grad}\mathcal{L}(\omega_{l,\iota}^t)^2 \right)^{\frac{1}{2}} \quad (20)$$

and

$$\rho(\omega_{G_l}^t) = \left(\sum_{\omega_{l,\iota}^t \in \mathbb{M}_{l,\iota} \in \mathcal{I}_{G_l}} \rho(\omega_{l,\iota}^t, \hat{\omega}_{l,\iota}) \right), \quad (21)$$

where $\omega_{G_l}^t = (\omega_1^t, \omega_2^t, \dots, \omega_{|\mathcal{I}_{G_l}|}^t)$. We employ a Taylor expansion on Ψ_t [41], [13], and we obtain

$$\Psi_{t+1} - \Psi_t \leq ((\rho_{G_l}^{t+1})^2 - (\rho_{G_l}^t)^2) \Psi_t' + ((\rho_{G_l}^{t+1})^2 - (\rho_{G_l}^t)^2)^2. \quad (22)$$

In order to compute the difference between $\rho_{G_l}^{t+1}$ and $\rho_{G_l}^t$, we employ a Taylor expansion on the geodesics [41], [13] by

$$\rho_{G_l}^{t+1} - \rho_{G_l}^t \leq \left(\frac{g(t, \Theta)}{\mathfrak{g}(\omega_{G_l}^t)} \right)^2 \|\text{grad}\mathcal{L}(\omega_{G_l}^t)\|_2^2 \kappa - 2 \left\langle h(\text{grad}\mathcal{L}(\omega_{G_l}^t), g(t, \Theta)), \phi_{\omega_{G_l}^t} (\hat{\omega}_{G_l})^{-1} \right\rangle,$$

where $\hat{\omega}_{G_l} = (\hat{\omega}_1, \hat{\omega}_2, \dots, \hat{\omega}_{|\mathcal{I}_{G_l}|})$, and $\kappa \leq \Upsilon_1$ where $\Upsilon_1 = 1 + \mathfrak{c}_{G_l}(\rho_{G_l}^t + R_{G_l}^t)$ is an upper bound on the operator norm of half of the Riemannian Hessian of $\rho(\cdot, \hat{\omega}_{G_l})^2$ along the geodesic joining $\omega_{G_l}^t$ and $\omega_{G_l}^{t+1}$. In order to explore asymptotic convergence, we define $\Omega_t = \{s_i\}_{i=1}^{t-1}$ to be an increasing sequence of σ algebras generated by samples that are processed before the t^{th} epoch. Since s_t is independent of Ω_t and $\omega_{G_l}^t$ is Ω_t measurable, we have

$$\mathbb{E}(h(\text{grad}\mathcal{L}(\omega_{G_l}^t), g(t, \Theta))^2 \kappa | \Omega_t) \leq \left(\frac{g(t, \Theta)}{\mathfrak{g}(\omega_{G_l}^t)} \right)^2 \mathbb{E}((R_{G_l}^t)^2 \Upsilon_1), \quad (23)$$

and

$$\mathbb{E}((\rho_{G_l}^{t+1})^2 - (\rho_{G_l}^t)^2 | \Omega_t) \leq 2 \frac{g(t, \Theta)}{\mathfrak{g}(\omega_{G_l}^t)} \left\langle \phi_{\omega_{G_l}^t} (\hat{\omega}_{G_l})^{-1}, \nabla \mathcal{L}(\omega_{G_l}^t) \right\rangle + g(t, \Theta)^2. \quad (24)$$

If $\mathfrak{g}(\omega_{G_l}^t) = \max\{1, \Gamma_1^t\}^{\frac{1}{2}}$, $\Gamma_1^t = (R_{G_l}^t)^2 \Gamma_2^t$, $\Gamma_2^t = \max\{(2\rho_{G_l}^t + R_{G_l}^t)^2, (1 + \mathfrak{c}_{G_l}(\rho_{G_l}^t + R_{G_l}^t))\}$, then we have

$$\mathbb{E}(\Psi_{t+1} - \Psi_t | \Omega_t) \leq \mathbb{E}((\rho_{G_l}^{t+1})^2 - (\rho_{G_l}^t)^2 | \Omega_t) \Psi_t' + g(t, \Theta)^2 \quad (25)$$

and

$$\mathbb{E}(\Psi_{t+1} - \Psi_t | \Omega_t) \leq 2 \frac{g(t, \Theta)}{\mathfrak{g}(\omega_{G_l}^t)} \left\langle \phi_{\omega_{G_l}^t} (\hat{\omega}_{G_l})^{-1}, \nabla \mathcal{L}(\omega_{G_l}^t) \right\rangle \Psi_t + g(t, \Theta)^2. \quad (26)$$

Thus, we have

$$\mathbb{E}(\Psi_{t+1} - \Psi_t | \Omega_t) \leq 2g(t, \Theta)^2, \quad (27)$$

and $\Psi_t + \sum_{t=0}^{\infty} g(t, \Theta)^2$ is a positive supermartingale, and converges almost surely. Since

$$\sum_{t=0}^{\infty} \mathbb{E}([\mathbb{E}(\Psi_{t+1} - \Psi_t | \Omega_t)^+]) \leq \sum_{t=0}^{\infty} g(t, \Theta)^2 < \infty, \quad (28)$$

we observe that Ψ_t is a quasi-martingale [41], [13], and thereby we have almost surely

$$-\sum_{t=0}^{\infty} \frac{g(t, \Theta)}{\mathfrak{g}(\omega_{G_l}^t)} \left\langle \phi_{\omega_{G_l}^t} (\hat{\omega}_{G_l})^{-1}, \nabla \mathcal{L}(\omega_{G_l}^t) \right\rangle \Psi_t < \infty. \quad (29)$$

Using properties of quasi-martingale [42], Ψ_t converges almost surely. In order to show almost sure convergence of $\nabla \mathcal{L}(\omega_{G_l}^t)$ to 0, we use Theorem 4.1 and 4.2 of [13]. For this purpose, we need to show that gradients of loss functions are bounded in compact sets of weights. Since

$$\inf_{\rho_{G_l}^t > \epsilon^{\frac{1}{2}}} \left\langle \phi_{\omega_{G_l}^t} (\hat{\omega}_{G_l})^{-1}, \nabla \mathcal{L}(\omega_{G_l}^t) \right\rangle < 0,$$

a weight $\omega_{G_l}^t$ is moved towards $\hat{\omega}_{G_l}$ by the gradient when $\rho_{G_l}^t > \epsilon^{\frac{1}{2}}$ where the set $\mathfrak{S} = \{\omega_{G_l}^t : \rho_{G_l}^t \leq \epsilon^{\frac{1}{2}}\}$ is a compact set. Since all continuous functions of $\omega_{G_l}^t \in \mathfrak{S}$ are bounded, and adaptive step size $\mathfrak{g}(\omega_{G_l}^t)$ satisfies $\frac{g(t, \Theta)}{\mathfrak{g}(\omega_{G_l}^t)} \leq g(t, \Theta)$ and $\mathfrak{g}(\omega_{G_l}^t)^2$ dominates $R_{G_l}^t$, we obtain that $\mathbb{E}(R_{G_l}^t)^2 \leq \mathfrak{K}$ for some $\mathfrak{K} > 0$ on a compact set \mathcal{K} . Thereby, we can show that conditions of Theorem 4.1 and 4.2 of [13] are satisfied. Therefore, we obtain almost sure convergence of $\nabla \mathcal{L}(\omega_{G_l}^t)$ to 0 by applying Theorem 4.1 and 4.2 in the rest of the proof. \square

Corollary 1. Suppose a DNN has loss functions whose local minima are also global minima. If the DNN is trained using the proposed FG-SGD and weight renormalization methods, then the loss of the DNN converges to global minima.

Proof. By Theorem 2, we assure that a loss function of a DNN which employs the proposed FG-SGD and weight renormalization methods for training converges to local minima. If the local minima is the global minima for the DNN, then the loss function converges to the global minima. \square

Corollary 2. Suppose that \mathbb{M}_l are identified by $n_l \geq 2$ dimensional unit sphere \mathbb{S}^{n_l} , and $\rho_{G_l}^t \leq \hat{c}^{-1}$, where \hat{c} is an upper bound on the sectional curvatures of $\mathbb{M}_{G_l}, \forall l$ at $\omega_{G_l}^t \in \mathbb{M}_{G_l}, \forall t$. If step size is computed using

$$h(\text{grad} \mathcal{L}(\omega_{G_l}^t), g(t, \Theta)) = -\frac{g(t, \Theta)}{\mathfrak{g}(\omega_{G_l}^t)} \text{grad} \mathcal{L}(\omega_{G_l}^t), \quad (30)$$

with $\mathfrak{g}(\omega_{G_l}^t) = (\max\{1, (R_{G_l}^t)^2(2 + R_{G_l}^t)^2\})^{\frac{1}{2}}$, then $\mathcal{L}(\omega_{G_l}^t) \xrightarrow[t \rightarrow \infty]{\text{a.s.}} \mathcal{L}(\hat{\omega}_{G_l})$, and $\nabla \mathcal{L}(\omega_{G_l}^t) \xrightarrow[t \rightarrow \infty]{\text{a.s.}} 0$, for each $\mathbb{M}_{G_l}, \forall l$. \blacksquare

Proof. If \mathbb{M}_{G_l} is a product of $n_l \geq 2$ dimensional unit spheres \mathbb{S}^{n_l} , then $\mathfrak{c}_{G_l} = 0$ and $\hat{c} = 1$ by Lemma 1. Thereby, Theorem 2 is applied to assure convergence by $\Gamma_t^1 = (R_{G_l}^t)^2(2 + R_{G_l}^t)^2$. \square

APPENDIX C EXPERIMENTAL DETAILS

We use three benchmark image classification datasets, namely Cifar-10, Cifar-100 and Imagenet [43], for analysis of convergence properties and performance of CNNs trained using FG-SGD. The Cifar-10 dataset consists of 60000 32×32 RGB images (50000 training images and 10000 test images) in 10 classes, with 6000 images per class. The Cifar-100 dataset consists of 100 classes containing 600 images each (500 training images and 100 testing images per class). The Imagenet (ILSVRC 2012) dataset consists of 1000 classes of 224×224 RGB images (1.2 million training images, 100000 test images and 50000 images used for validation).

A. Computational Complexity of Algorithm 1

Compared to SGD algorithms that use weights belonging to linear weight spaces [44], [45], the computational complexity of Algorithm 1 is dominated by computation of the maps Π and ϕ at line 6 and 9, depending on the structure of the weight manifold used at the l^{th} layer. Concisely, the computational complexity of Π is determined by computation of different norms that identify the manifolds. For instance, for the sphere, we use $\Pi_{\omega_t^t} \mu_t \triangleq (1 - \|\omega_t^t\|_F^2) \mu_t$. Thereby, for an $A \times A$ weight, the complexity is bounded by $O(A^3)$, where $O(\cdot)$ denotes an asymptotic upper bound [46]. Similarly, the computational complexity of ϕ depends on the manifold structure. For example, the exponential maps on the sphere and the oblique manifold can be computed using functions of \sin and \cos functions, while that on the Stiefel manifold is a function of matrix exponential. For computation of matrix exponential, various numerical approximations with $O(\epsilon A^3)$ complexity were proposed for different approximation order ϵ [42], [47], [48], [49]. However, unit norm matrix normalization is used for computation of retractions on the sphere and the oblique manifold. Moreover, QR decomposition of matrices is computed with $O(A^3)$ [50] for retractions on the Stiefel manifold. In addition, computation time of maps can be reduced using parallel computation methods. For instance, a rotation method was suggested to compute QR using $O(A^2)$ processors in $O(A)$ unit time in [51]. Therefore, computation of retractions is computationally less complex compared to that of the exponential maps. Since the complexity analysis of these maps is beyond the scope of this work, and they provide the same convergence properties for our proposed algorithm, we used the retractions in the experiments. Implementation details are given in the next section.

1) *A Discussion on Implementation of Algorithm 1 in Parallel and Distributed Computing Systems:* In the experiments, algorithms are implemented using GPU and CPU servers consisting of GTX 2070, GTX 1080, GTX-Titan-X, GTX-Titan-Black, Intel i7-5930K, Intel Xeon E5-1650 v3 and E5-2697 v2. Since we used hybrid GPU and CPU servers in the experiments, and a detailed analysis of parallel and distributed computation methods of CNNs is beyond the scope of this work, we report bounds on average running times of SGD algorithms in this section.

In the implementation of linear Euclidean SGD methods, we use vectorized computation of weight updates. Therefore, we use large scale matrix computation methods (in some cases, for sparse matrices) to improve running time of the linear Euclidean SGD methods. However, we deal with optimization using batched (small size) dense matrices in the implementation of Algorithm 1 [52]. Therefore, in order to improve running time of the algorithm, we implemented Algorithm 1 using hybrid CPU-GPU programming paradigms.

More precisely, we consider two computation schemes according to matrix/tensor structure of the weights, i.e. geometric structure of weight manifolds. First, we recall that we construct different manifolds of weights $\mathcal{W} = \{\mathbf{W}_{d,l} \in \mathbb{R}^{A_l \times B_l \times C_l}\}_{d=1}^{D_l}, \forall l = 1, 2, \dots, L$, at different layers of an L -layer CNN. Then, we implement projections of gradients and retractions at

- 1) Fully Connected (FC) layers at which we use $\mathbf{W}_l^{fc} \in \mathbb{R}^{C_l \times D_l}$ with $A_l = B_l = 1$, and
- 2) Convolution (Conv) layers at which we use $\mathbf{W}_{d,l} \in \mathcal{W}$ with $A_l > 1$ and $B_l > 1$.

At the FC layers, we implemented Algorithm 1 on GPUs using Cuda with Cublas and Magma [53], [54], [55] Blas [56], [57]. In the experimental analyses, we obtained similar running times using Cublas

and Magma Blas implementation of Algorithm 1 (denoted by \mathcal{R}_M^{fc}) compared to running time of linear Euclidean SGD (denoted by \mathcal{R}_E^{fc}), for each epoch.

For instance, if we train CNNs using the Cifar-100 dataset and one GTX 1080, then we observe $\mathcal{R}_M^{fc} < \alpha \mathcal{R}_E^{fc}$, where the running times are bounded by $\alpha > 0$ due to implementation of gradient projections and retractions. The overhead factor α also depends on the manifold structure of the weights such that $\alpha < 1.5$ for the sphere, $\alpha < 2.5$ for the oblique manifold and $\alpha < 5$ for the Stiefel manifold.

When we implemented a QR decomposition algorithm using the Givens transformation (Rotation) [58], [50], we obtained further improvement by $\alpha < 4$. In addition, batch size does not affect the overhead of running time crucially as long as the GPU memory is sufficient. The effect of this overhead on the overall training time depends on structure of CNNs. For example, we use multiple (6) FC layers in NiNs where we have 2 FC layers in SKs. Therefore, the overhead affects the training time of NiNs more than that of SKs.

At the Conv layers, we implemented Algorithm 1 on both GPUs and CPUs. However, the structure of parallelization of projections and maps at the Conv layers is different than that of projections and maps computed at the FC layers. More precisely, we perform parallel computation either 1) using tensors $\mathbf{W}_{d,l} \in \mathbb{R}^{A_l \times B_l \times C_l}$ for each output $d = 1, 2, \dots, D_l$, or 2) using matrices $W_{c,d,l} \in \mathbb{R}^{A_l \times B_l}$ for each output $d = 1, 2, \dots, D_l$ and channel $c = 1, 2, \dots, C_l$.

Since there is an I/O bottleneck between transfer of matrices and tensors to/from GPUs from/to CPUs, we used either (1) or (2) according to output size D_l , and channel size C_l . For instance, if $C_l > D_l$, then we performed computations on GPUs. Otherwise, we implemented the algorithm on multi-core CPUs.

In average, for an epoch⁹, the running time of a GPU implementation of Algorithm 1 for the case (1) denoted by $\mathcal{R}_{M,gpu}^1$, and that of linear Euclidean SGD for the case $\mathcal{R}_{E,gpu}^1$ are related by $\mathcal{R}_{E,gpu}^1 < \alpha \mathcal{R}_{M,gpu}^1$ for $\alpha < 3$ for the sphere and $\alpha < 3$ for the oblique manifold and $\alpha < 6$ for the Stiefel manifold¹⁰. The additional computational overhead can be attributed to additional transmission time and computation of multi-dimensional transpose operations.

Moreover, we observed that the running time of the multi-core CPU implementation of the algorithm $\mathcal{R}_{M,cpu}^1$ is bounded by $\mathcal{R}_{M,gpu}^1 < \alpha \mathcal{R}_{M,cpu}^1$ for $\alpha < f(D_l) < 10$, where $f(\cdot)$ is a function of number of output D_l for all manifolds¹¹. In other words, the difference between running times on CPUs and GPUs is affected by D_l more than the other parameters $2 \leq A_l \leq 7$ and $2 \leq B_l \leq 7$, and C_l . This observation can be attributed to the less overhead between Blas and Cublas implementations of matrix operations for small number (e.g. $C_l < 10^3$) of weight matrices.

For the second case where $C_l > D_l$, we observed that $\mathcal{R}_{E,gpu}^1 < \alpha_1 \mathcal{R}_{M,cpu}^1 < \alpha_2 \mathcal{R}_{M,gpu}^1$. We observed that $\alpha_1 < \hat{f}(C_l, D_l) < 2$ and $\alpha_2 < \hat{f}(C_l, D_l) < 5$, where $\hat{f}(\cdot, \cdot)$ is a function of both C_l and D_l , for the sphere, and scales for the other manifolds accordingly, for implementation using one GTX 1080 and E5-2697 v2.

B. Implementation Details of Algorithm 1

In this section, we give implementation details of Algorithm 1.

1) *Identification of Component Kernel Submanifolds of POMs*: We identify component weight manifolds \mathcal{M}_l of POMs \mathbb{M}_{G_l} at each l^{th} of an L -layer CNN, and initialize weights residing in the manifolds considering both statistical properties of data, and geometric properties of weight manifolds.

In the experiments, we used the sphere, the oblique manifold and the Stiefel manifold to construct component weight manifolds according to definition of manifolds given in Table V.

⁹For the example of training using the Cifar-100 dataset given above.

¹⁰For different implementations of QR decomposition on GPUs, we observed $3 < \alpha < 6$.

¹¹We observed that for Intel Xeon E5-1650 v3, and obtained improvement of running time by approximately $f(D_l) < 5$ for E5-2697 v2 since using larger number of CPU cores.

TABLE VII: Tangent spaces and maps used for orthogonal projection of Euclidean gradients obtained using backpropagation onto the tangent spaces for the manifolds of the normalized weights defined in Table V. We denote a vector realized by a Euclidean gradient obtained at a weight $\omega_{G_l}^t$ from the $l + 1^{st}$ layer using backpropagation by $\mu \triangleq \left(\text{grad}_E \mathcal{L}(\omega_{g,l}^t), \Theta, \mathcal{R}_l^t \right)$ (see Line 5 of Algorithm 1).

Manifolds	Tangent Spaces	Projection of Gradients
$\mathcal{S}(A_l, B_l)$	$T_\omega \mathcal{S}(A_l, B_l) = \{\hat{\omega} \in \mathbb{R}^{A_l \times B_l} : \omega^T \hat{\omega} = 0\}$	$\Pi_\omega \mu = (I - \omega \omega^T) \mu$
$\mathcal{OB}(A_l, B_l)$	$T_\omega \mathcal{OB}(A_l, B_l) = \{\hat{\omega} \in \mathbb{R}^{A_l \times B_l} : \omega^T \hat{\omega} = 0\}$	$\Pi_\omega \mu = \mu - \omega \text{ddiag}(\omega^T \mu)$
$\mathcal{St}(A_l, B_l)$	$T_\omega \mathcal{St}(A_l, B_l) = \{\hat{\omega} \in \mathbb{R}^{A_l \times B_l} : \text{ddiag}(\omega^T \hat{\omega}) = 0\}$	$\Pi_\omega \mu = (I - \omega \omega^T) \mu + \omega \zeta(\omega^T \mu)$

TABLE VIII: Exponential maps and retractions for the manifolds of the normalized weights defined in Table V. We denote a vector moved on a tangent space at the t^{th} epoch by v_t (see Line 8 of Algorithm 1). In addition, $\varkappa(Z)$ is the unit-norm normalization of each column of a matrix Z . $\mathcal{Q}_{\mathcal{F}}(Z) := Q$ is the Q factor of the QR decomposition $Z = QR$ of Z .

Manifolds	Exponential Maps	Retraction
$\mathcal{S}(A_l, B_l)$	$\exp_\omega(v) = \omega \cos(\ v\ _F) + \frac{v}{\ v\ _F} \sin(\ v\ _F)$	$\mathfrak{R}_\omega(v) = \frac{\omega + v}{\ \omega + v\ _F}$
$\mathcal{OB}(A_l, B_l)$	$\exp_\omega(v) = \omega \text{ddiag}(\cos(\ v\ _F)) + v \text{ddiag}(\frac{\sin(\ v\ _F)}{\ v\ _F})$	$\mathfrak{R}_\omega(v) = \varkappa(\omega + v)$
$\mathcal{St}(A_l, B_l)$	$\exp_\omega(v) = [\omega \ v] \hat{\text{exp}} \left(\begin{bmatrix} \omega^T v & -v^T v \\ I & \omega^T v \end{bmatrix} \right) \begin{bmatrix} I \\ 0 \end{bmatrix} \hat{\text{exp}}(-\omega^T v)$	$\mathfrak{R}_\omega(v) = \mathcal{Q}_{\mathcal{F}}(\omega + v)$

2) *Computation of Gradient Maps, Projections and Retractions used in Algorithm 1:* In this section, we provide the details of the methods used for computation of gradient maps, projections and retractions for different collections of POMs in Algorithm 1. We denote a vector moved on a tangent space at the t^{th} epoch by v_t (see Line 7 of Algorithm 1). In addition, $\varkappa(Z)$ is the unit-norm normalization of each column of a matrix Z . $\mathcal{Q}_{\mathcal{F}}(Z) := Q$ is the Q factor of the QR decomposition $Z = QR$ of Z .

Definitions of component manifolds of POMs used in this work are given in Table V. In Table VII, we provide tangent spaces and maps used for orthogonal projection of Euclidean gradients onto the tangent spaces for the manifolds of the normalized weights which are defined in Table V. Exponential maps and retractions are given in Table VIII.

We also note that various types of projections, exponential maps and retractions can be computed and used in Algorithm 1 in addition to the projections, maps and retractions given in the tables. More detailed discussion on their computation are given in [59], [60], [26].

C. Implementation Details of CNN Architectures used in the Experiments

Data pre-processing and post-processing: For the experiments on Cifar-10 and Cifar-100 datasets, we used two standard data augmentation techniques which are horizontal flipping and translation by 4 pixels [44], [61].

For the experiments on Imagenet dataset, we followed the data augmentation methods suggested in [44]. In addition, we used both the scale and aspect ratio augmentation used in [62]. For color augmentation, we used the photometric distortions [63] and standard color augmentation [44]. Moreover, we used random

sampling of 224×224 crops or their horizontal flips with the normalized data obtained by subtracting per-pixel mean. In the bottleneck blocks, stride 2 is used for the $A_l = B_l = 3$ weights. Moreover, Euclidean gradient decays are employed for all the weights.

Acceleration methods: In this section, we employed state-of-the-art acceleration methods [64] modularly in Algorithm 1 for implementation of the CNNs as suggested in the reference works [44], [61], [13]. In this work, we consider employment of acceleration methods on the ambient Euclidean space and collections of POMs as suggested in [13]. For this purpose, momentum and Euclidean gradient decay methods are employed on the Euclidean gradient $\text{grad}_E \mathcal{L}(\omega_{g,l}^t)$ using $\mu_t := q(\text{grad}_E \mathcal{L}(\omega_{g,l}^t), \mu_t, \Theta)$. We can employ state-of-the-art acceleration methods [64] modularly in this step. Thus, momentum was employed with the Euclidean gradient decay using

$$q(\text{grad}_E \mathcal{L}(\omega_{g,l}^t), \mu_t, \Theta) = \theta_\mu \mu_t - \theta_E \text{grad}_E \mathcal{L}(\omega_{g,l}^t), \quad (31)$$

where $\theta_\mu \in \Theta$ is the parameter employed on the momentum variable μ_t . We consider $\theta_E \in \Theta$ as the decay parameter for the Euclidean gradient. In the experiments, we used $\theta_\mu = \theta_E = 0.9$.

Architectural Details of CNNs: In the experiments, we used the same hyper-parameters of CNN architectures (e.g. number of channels, layers, weight sizes, stride and padding parameters) and their implementation provided by the authors of the compared works for training of CNNs using our proposed SGD method, for a fair comparison with base-line methods. Differences between the implementations and hyper-parameters are explained below. In other words, we just implemented the SGD algorithm of the provided CNN implementations using our proposed SGD method. More precisely, we used the following implementations for comparison:

- RCD and RSD: We used the Residual networks with constant and stochastic depth using the same configuration hyper-parameters (see below for number of weights used in the architectures) and code given in [61].
- Residual Networks (Resnets): We re-implemented residual networks with the same configuration and training hyper-parameters (see below for number of weights used in the architectures) given in [44], [13].
- Squeeze-and-Excitation networks implemented for Resnets with 50 layers (SENet-Resnet-50): We re-implemented residual networks with the same configuration and training hyper-parameters (see below for number of weights used in the architectures) given in [37].

In order to construct collections of weights belonging to four spaces (Euc., Sp, St and Ob) using WSS, we increase the number of weights used in CNNs to 24 and its multiples as follows;

- Resnet with 18 Layers (Table 6 in this text): 72 filters at the first and second, 144 filters at the third, 288 filters at the fourth, and 576 filters at the fifth convolution blocks [44].
- Resnet with 44 Layers (Table 7 in this text): 24 filters for 15 layers, 48 filters for 14 layers, 96 filters for 14 [44].
- Resnets with constant depth (RCD) and stochastic depth (RSD) with 110 layers (Table 2 in the main text and Table 8 in this text): 24, 48 and 72 filters at the first, second, and the third convolution blocks [61].
- Resnet-50 and SENet-Resnet-50 (Table 1 in the main text): Configurations of Resnet-50 and SENet-Resnet-50 are given in Table IX and Table X, respectively.

Scaling of weights: We use \mathfrak{R}_l^t for scaling of weights and identification of component weight manifolds of POMs. As we mentioned in the main text, for instance, \mathfrak{R}_l^t is computed and used as the radius of the sphere. More precisely, we initialize weights $\omega \in \mathcal{M}_l$ that belong to the sphere $\mathcal{M}_l \equiv \mathcal{S}(A_l, B_l)$ subject to the constraint $\|\omega\|_F^2 = \mathfrak{R}_l^t$ by constructing a scaled sphere

$$\mathbb{S}^{A_l B_l - 1} \triangleq \mathcal{S}_{\mathfrak{R}_l^t}(A_l, B_l) = \{\omega \in \mathbb{R}^{A_l \times B_l} : \|\omega\|_F^2 = \mathfrak{R}_l^t\}. \quad (32)$$

The other manifolds (the oblique and the Stiefel manifolds) are identified, and the weights that belong to the manifolds are initialized, appropriately, following the aforementioned methods. Then, projection

TABLE IX: Configuration details of the Resnet-50 used for the experiments given in Table 1 in the main text.

Output Size	Resnet-50
112 × 112	Kernel size: 7 × 7, Number of convolution weights: 64, Stride 2
56 × 56	3 × 3 Max Pooling, Stride 2 3 Residual Blocks with the Following Convolution Kernels: 72 convolution weights of size 1 × 1 72 convolution weights of size 3 × 3 264 convolution weights of size 1 × 1
28 × 28	4 Residual Blocks with the Following Convolution Kernels: 144 convolution weights of size 1 × 1 144 convolution weights of size 3 × 3 528 convolution weights of size 1 × 1
14 × 14	6 Residual Blocks with the Following Convolution Kernels: 264 convolution weights of size 1 × 1 264 convolution weights of size 3 × 3 1032 convolution weights of size 1 × 1
7 × 7	3 Residual Blocks with the Following Convolution Kernels: 528 convolution weights of size 1 × 1 528 convolution weights of size 3 × 3 2064 convolution weights of size 1 × 1
1 × 1	Global Average Pooling Fully connected layer Softmax

of gradients, exponential maps and retractions which are determined according to manifold structure of weight spaces (see Table VII and Table VIII), are updated accordingly by \mathfrak{R}_l^t . For example, for the scaled sphere $\mathcal{S}_{\Gamma_l^t}(A_l, B_l)$, we compute the projection of gradients by $(I\mathfrak{R}_l^t - \omega\omega^T)\mu$, and the exponential map by

$$\exp_{\omega}(v) = \omega \cos(\|v\|_F \mathfrak{R}_l^t) + \mathfrak{R}_l^t \frac{v}{\|v\|_F} \sin(\|v\|_F \mathfrak{R}_l^t). \quad (33)$$

TABLE X: Configuration details of the SENet-Resnet-50 used for the experiments given in Table 1 in the main text.

Output Size	Resnet-50
112 × 112	Kernel size: 7 × 7, Number of convolution weights: 64, Stride 2
56 × 56	3 × 3 Max Pooling, Stride 2 3 Residual Blocks with the Following Convolution Kernels: 72 convolution weights of size 1 × 1 72 convolution weights of size 3 × 3 264 convolution weights of size 1 × 1 Fully connected layer with weights of size 24 × 264
28 × 28	4 Residual Blocks with the Following Convolution Kernels: 144 convolution weights of size 1 × 1 144 convolution weights of size 3 × 3 528 convolution weights of size 1 × 1 Fully connected layer with weights of size 48 × 528
14 × 14	6 Residual Blocks with the Following Convolution Kernels: 264 convolution weights of size 1 × 1 264 convolution weights of size 3 × 3 1032 convolution weights of size 1 × 1 Fully connected layer with weights of size 72 × 1032
7 × 7	3 Residual Blocks with the Following Convolution Kernels: 528 convolution weights of size 1 × 1 528 convolution weights of size 3 × 3 2064 convolution weights of size 1 × 1 Fully connected layer with weights of size 144 × 2064
1 × 1	Global Average Pooling Fully connected layer Softmax

D. Employment of Weight Set Splitting Scheme (WSS) in the Experiments:

Recall that, at each l^{th} layer, we compute a weight $\omega_l \triangleq W_{c,d,l}$, $c \in \Lambda^l$, $\Lambda^l = \{1, 2, \dots, C_l\}$, $d \in O^l$, $O^l = \{1, 2, \dots, D_l\}$. We first choose \mathfrak{A} subsets of indices of input channels $\Lambda_a \subseteq \Lambda^l$, $a = 1, 2, \dots, \mathfrak{A}$, and \mathfrak{B} subsets of indices of output channels $O_b \subseteq O^l$, $b = 1, 2, \dots, \mathfrak{B}$, such that $\Lambda^l = \bigcup_{a=1}^{\mathfrak{A}} \Lambda_a$ and $O^l = \bigcup_{b=1}^{\mathfrak{B}} O_b$. We determine indices of weights belonging to different groups using the following three schemes:

- 1) POMs for input channels (PI): For each c^{th} input channel, we construct $\mathcal{I}_{G_l} = \bigcup_{c=1}^{C_l} \mathcal{I}_{G_l}^c$, where $\mathcal{I}_{G_l}^c = O_b \times \{c\}$ and the Cartesian product $O_b \times \{c\}$ preserves the input channel index, $\forall b, c$ (see Figure 1).
- 2) POMs for output channels (PO): For each d^{th} output channel, we construct $\mathcal{I}_{G_l} = \bigcup_{d=1}^{D_l} \mathcal{I}_{G_l}^d$, where $\mathcal{I}_{G_l}^d = \Lambda_a \times \{d\}$ and the Cartesian product $\Lambda_a \times \{d\}$ preserves the output channel index, $\forall a, d$ (see Figure 1).
- 3) POMs for input and output channels (PIO): In PIO, we construct $\mathcal{I}_l^{a,b} = \mathcal{I}_l^a \cup \mathcal{I}_l^b$, where $\mathcal{I}_l^a = \{\Lambda_a \times a\}$, and $\mathcal{I}_l^b = \{O_b \times b\}$ such that $\mathcal{I}_{G_l} = \bigcup_{a=1, b=1}^{\mathfrak{A}, \mathfrak{B}} \mathcal{I}_l^{a,b}$ (see Figure 1).

Illustrative Examples of Employment of PI, PO and PIO

A comparative and illustrative example for comparison of PI, PO and PIO is given in Figure 1.

Example 1. Suppose that we have a weight tensor of size $3 \times 3 \times 4 \times 6$ where the number of input and output channels is 4 and 6. In total, we have $4 * 6 = 24$ weight matrices of size 3×3 . An example of construction of an collection of POMs is as follows.

- 1) PIO: We split the set of 24 weights into 10 subsets. For 6 output channels, we split the set of weights

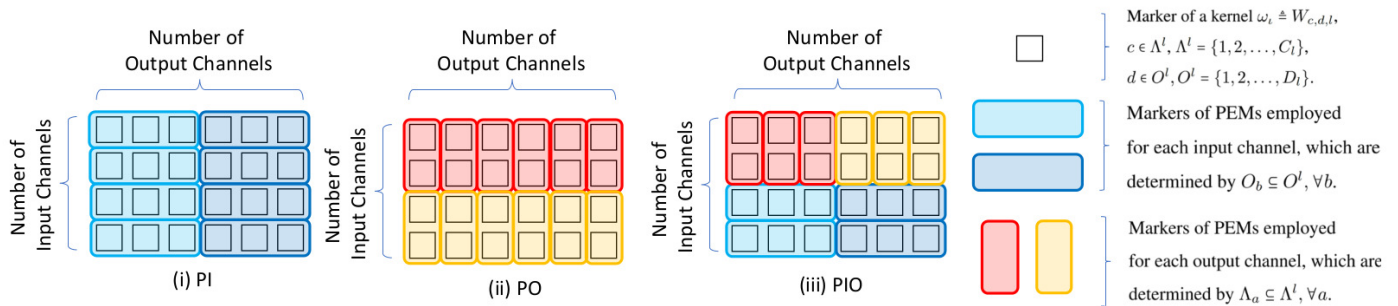


Fig. 1: An illustration for employment of the proposed PI, PO and PIO strategies at the l^{th} layer of a CNN.

corresponding to 4 input channels into 3 subsets. We choose the sphere (Sp) for 2 subsets each containing 3 weights (depicted by light blue rectangles), and 3 subsets each containing 2 weights (depicted by red rectangles). We choose the Stiefel manifold (St) similarly for the remaining subsets. Then, our ensemble contains 5 POMs of St and 5 POMs of Sp.

- 2) PI: For each of 4 input channels, we split a set of 6 weights associated with 6 output channels into two subsets of 3 weights. Choosing the sphere (Sp) for the first subset, we construct a POM as a product of 3 Sp. That is, each of 3 component manifolds $\mathcal{M}_\ell, \ell = 1, 2, 3$, of the POM is a sphere. Similarly, choosing the Stiefel (St) for the second subset, we construct another POM as a product of 3 St (each of 3 component manifolds $\mathcal{M}_\ell, \ell = 1, 2, 3$, of the second POM is a Stiefel manifold.). Thus, at this layer, we construct an collection of 4 POMs of 3 St and 4 POMs of 3 Sp.
- 3) PO: For each of 6 output channels, we split a set of 4 weights corresponding to the input channels into two subsets of 2 weights. We choose the Sp for the first subset, and we construct a POM as a product of 2 Sp using. We choose the St for the second subset, and we construct a POM as a product of 2 St. Thereby, we have an collection consisting of 6 POMs of St and 6 POMs of Sp.

In the experiments, indices of weights for PI, PO and PIO are randomly selected. An illustration of the selection method is given in Figure 2.

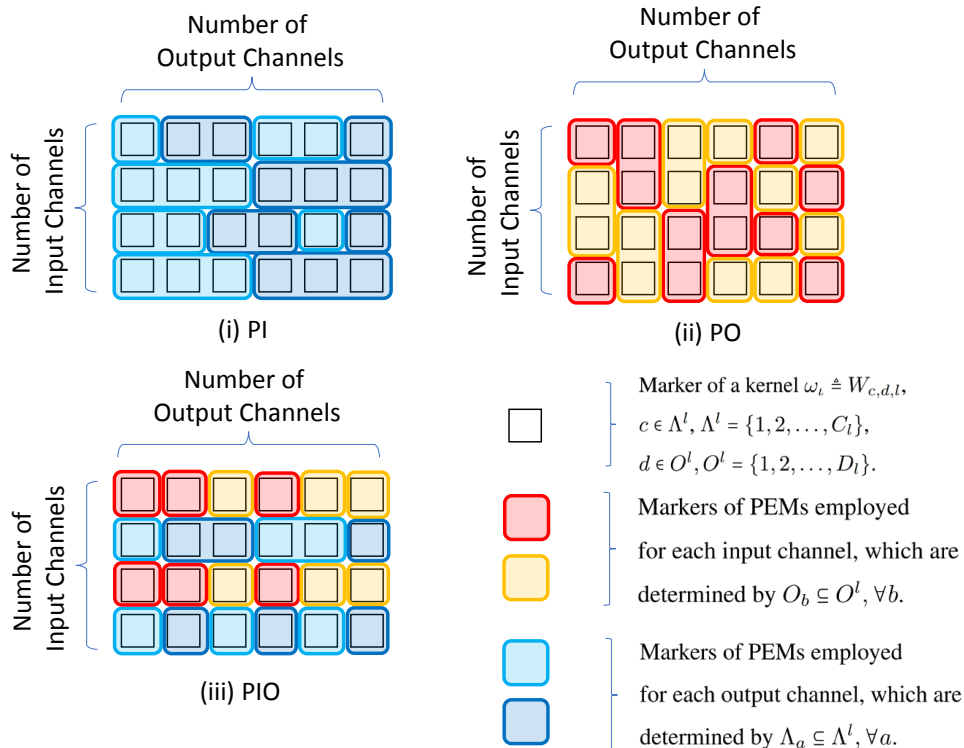


Fig. 2: An illustration of employment of the proposed PI, PO and PIO collection strategies at the l^{th} layer of a CNN. In Section 4.2, we randomly selected indices of weights, i.e. subsets of input and output channels, according to the uniform distribution. In this example, we suppose that there are four input and six output channels. Then, 24 convolution weights are computed on in two different POMs.

Notation used in the Tables

- 1) Sp/Ob/St: Kernels employed on each input and output channel are defined to reside on the sphere, oblique and Stiefel manifold, respectively.
- 2) POMs of Sp/Ob/St: Kernels employed on all input and output channels are defined to reside on a POM of Sp/Ob/St.
- 3) PI/PO/PIO for POMs of Sp/Ob/St: Ensembles of POMs of Sp/Ob/St are computed using the schemes PI/PO/PIO.
- 4) Results for $\text{Manifold}_1 + \text{Manifold}_2$: Results are computed for collections of POMs of Manifold_1 and Manifold_2 .
- 5) Results for $\text{Manifold}_1 + \text{Manifold}_2 + \text{Manifold}_3$: Results are computed for collections of POMs of Manifold_1 , Manifold_2 and Manifold_3 .
- 6) Results for $\text{Manifold}_1 + \text{Manifold}_2 + \text{Manifold}_3 + \text{Manifold}_4$: Results are computed for collections of POMs of Manifold_1 , Manifold_2 , Manifold_3 and Manifold_4 .

APPENDIX D ADDITIONAL RESULTS

A. Analyses using Resnets with Different Number of Layers

In this subsection, we give additional results for image classification using Cifar-10 and Imagenet datasets for different networks such as Resnets with 18 and 44 layers (Resnet-18 and Resnet-44), 110-layer Resnets with constant depth (RCD) and stochastic depth (RSD) with data augmentation (DA) and without using data augmentation (w/o DA).

TABLE XI: Results for Resnet-18 which are trained using the Imagenet for single crop validation error rate (%).

Model	Top-1 Error (%)
Euc. [13]	30.59
Euc. †	30.31
Sp/Ob/St[13]	29.13/28.97/28.14
Sp/Ob/St †	28.71/28.83/28.02
POMs of Sp/Ob/St	28.70/28.77/28.00
PI for POMs of Sp/Ob/St	28.69/28.75/27.91
PI (Euc.+Sp/Euc.+St/Euc.+Ob)	30.05/29.81/29.88
PI (Sp+Ob/Sp+St/Ob+St)	28.61/28.64/28.49
PI (Sp+Ob+St/Sp+Ob+St+Euc.)	27.63/27.45
PO for POMs of Sp/Ob/St	28.67/28.81/27.86
PO (Euc.+Sp/Euc.+St/Euc.+Ob)	29.58/29.51/29.90
PO (Sp+Ob/Sp+St/Ob+St)	28.23/28.01/28.17
PO (Sp+Ob+St/Sp+Ob+St+Euc.)	27.81/27.51
PIO for POMs of Sp/Ob/St	28.64/28.72/27.83
PIO (Euc.+Sp/Euc.+St/Euc.+Ob)	29.19/28.25/28.53
PIO (Sp+Ob/Sp+St/Ob+St)	28.14/27.66/27.90
PIO (Sp+Ob+St/Sp+Ob+St+Euc.)	27.11/ 27.07

We give classification performance of Resnets with 18 layers (Resnet-18) employed on the Imagenet in Table XI. The results show that performance of CNNs are boosted by employing collections of POMs (denoted by PIO for POMs) using FG-SGD compared to the employment of baseline Euc. We observe that POMs of component manifolds of identical geometry (denoted by POMs of Sp/St/Ob), and their collections (denoted by PIO for POMs of Sp/St/Ob) provide better performance compared to employment of individual component manifolds (denoted by Sp/Ob/St) [13]. For instance, we obtain 28.64%, 28.72% and 27.83% error using PIO for POMs of Sp, Ob and St in Table XI, respectively. However, the error obtained using Sp, Ob and St is 28.71%, 28.83% and 28.02%, respectively. We observe 3.24% boost by construction of an collection of four manifolds (Sp+Ob+St+Euc.) using the PIO scheme in Table XI (27.07%). In other words, collection methods boost the performance of large-scale CNNs more for large-scale datasets (e.g. Imagenet) consisting of larger number of samples and classes compared to the performance of smaller CNNs employed on smaller datasets (e.g. Cifar-10). This result can be attributed to enhancement of sets of features learned using multiple constraints.

In addition, we obtain 0.28% and 2.06% boost of the performance by collection of the St with Euc. (6.77% and 28.25% using PIO for Euc.+St, respectively) for the experiments on the Cifar-10 and Imagenet datasets using the PIO scheme in Table XII and Table XI, respectively. Moreover, we observe that construction of collections using Ob performs better for PI compared to PO. For instance, we observe that PI for POMs of Ob provides 6.81% and 28.75% while PO for POMs of Ob provides 6.83% and 28.81% in Table XII and Table XI, respectively. We may associate this result with the observation that weights belonging to Ob are used for feature selection and modeling of texture patterns with high performance [59], [65]. However, collections of St and Sp perform better for PO (6.59% and 28.01% in Table XII and Table XI) compared to PI (6.67% and 28.64% in Table XII and Table XI) on weights employed on output channels.

It is also observed that PIO performs better than PI and PO in all the experiments. We observe 3.24% boost by construction of an collection of four manifolds (Sp+Ob+St+Euc.) using the PIO scheme in Table XI (27.07%). In other words, collection methods boost the performance of large-scale CNNs more for large-scale datasets (e.g. Imagenet) consisting of larger number of samples and classes compared to the performance of smaller CNNs employed on smaller datasets (e.g. Cifar-10). This result can be attributed to enhancement of sets of features learned using multiple constraints.

In Table XIII, we analyze the performance of larger CNNs consisting of 110 layers on Cifar-100 with and without using DA. We implemented the experiments 10 times and provided the average performance. We

TABLE XII: Results for Resnet-44 on the Cifar-10 with DA.

Model	Class. Error(%)
Euc. [44]	7.17
Euc. [13]	7.16
Euc. †	7.05
Sp/Ob/St [13]	6.99/6.89/6.81
Sp/Ob/St †	6.84/6.87/ 6.73
POMs of Sp/Ob/St	6.81/6.85/ 6.70
PI for POMs of Sp/Ob/St	6.82/6.81/ 6.70
PI (Euc.+Sp/Euc.+St/Euc.+Ob)	6.89/6.84/6.88
PI (Sp+Ob/Sp+St/Ob+St)	6.75/6.67/6.59
PI (Sp+Ob+St/Sp+Ob+St+Euc.)	6.31/6.34
PO for POMs of Sp/Ob/St	6.77/6.83/ 6.65
PO (Euc.+Sp/Euc.+St/Euc.+Ob)	6.85/6.78/6.90
PO (Sp+Ob/Sp+St/Ob+St)	6.62/6.59/6.51
PO (Sp+Ob+St/Sp+Ob+St+Euc.)	6.35/6.22
PIO for POMs of Sp/Ob/St	6.71/6.73/ 6.61
PIO (Euc.+Sp/Euc.+St/Euc.+Ob)	6.95/6.77/6.82
PIO (Sp+Ob/Sp+St/Ob+St)	6.21/6.19/6.25
PIO (Sp+Ob+St/Sp+Ob+St+Euc.)	5.95/ 5.92

TABLE XIII: Classification error (%) for training 110-layer Resnets with constant depth (RCD) and Resnets with stochastic depth (RSD) using the PIO scheme on Cifar-100, with data augmentation (w. DA) and without using DA (w/o DA).

Model	Cifar-100 w. DA	Cifar-100 w/o DA
RCD [66]	27.22	44.74
(Euc.) †	27.01	44.65
Sp/Ob/St ([13])	26.44/25.99/25.41	42.51/42.30/40.11
Sp/Ob/St †	26.19/25.87/25.39	42.13/42.00/39.94
POMs of Sp/Ob/St	25.93/25.74/25.18	42.02/42.88/39.90
PIO (Euc.+Sp/Euc.+St/Euc.+Ob)	25.57/25.49/25.64	41.90/41.37/41.85
PIO (Sp+Ob/Sp+St/Ob+St)	24.71/24.96/24.76	41.49/40.53/40.34
PIO (Sp+Ob+St/Sp+Ob+St+Euc.)	23.96/ 23.79	39.53/ 39.35
RSD [66]	24.58	37.80
Euc. †	24.39	37.55
Sp/Ob/St [13]	23.77/23.81/23.16	36.90/36.47/35.92
Sp/Ob/St †	23.69/23.75/23.09	36.71/36.38/35.85
POMs of Sp/Ob/St	23.51/23.60/23.85	36.40/36.11/35.53
PIO (Euc.+Sp/Euc.+St/Euc.+Ob)	23.69/23.25/23.32	35.76/35.55/35.81
PIO (Sp+Ob/Sp+St/Ob+St)	22.84/22.91/22.80	35.66/35.01/35.35
PIO (Sp+Ob+St/Sp+Ob+St+Euc.)	22.19/ 22.03	34.49/ 34.25

observe that sets boost the performance of CNNs that use DA methods more compared to the performance of CNNs without using DA. For instance, PIO of all manifolds (**39.35%**) outperform baseline (**44.65%**) by 5.3% without using DA, while those (**23.79%**) obtained using DA outperform baseline (**27.01%**) by 3.22% for RCD. Additional results for different CNNs using Imagenet and Cifar-10, and a comparison with vanilla network sets are given in this supplemental material.

TABLE XIV: Classification error (%) for training 110-layer Resnets with constant depth (RCD) and Resnets with stochastic depth (RSD) using the PIO scheme on the Cifar-10, with and without using DA.

Model	Cifar-10 w. DA	Cifar-10 w/o DA
RCD [66]	6.41	13.63
(Euc.) †	6.30	13.57
Sp/Ob/St ([13])	6.22/6.07/5.93	13.11/12.94/12.88
Sp/Ob/St †	6.05/6.03/5.91	12.96/12.85/12.79
POMs of Sp/Ob/St	6.00/6.01/5.86	12.74/12.77/12.74
PIO for POMs of Sp/Ob/St	5.95/5.91/5.83	12.71/12.72/12.69
PIO (Euc.+Sp/Euc.+St/Euc.+Ob)	6.03/5.99/6.01	12.77/12.21/12.92
PIO (Sp+Ob/Sp+St/Ob+St)	5.97/5.86/5.46	11.47/11.65/ 11.51
PIO (Sp+Ob+St/Sp+Ob+St+Euc.)	5.25/5.17	11.29/11.15
RSD [66]	5.23	11.66
Euc. †	5.17	11.40
Sp/Ob/St [13]	5.20/5.14/4.79	10.91/10.93/10.46
Sp/Ob/St †	5.08/5.11/4.73	10.52/10.66/10.33
POMs of Sp/Ob/St	5.05/5.08/4.69	10.41/10.54/10.25
PIO for POMs of Sp/Ob/St	4.95/5.03/4.62	10.37/10.51/10.19
PIO (Euc.+Sp/Euc.+St/Euc.+Ob)	5.00/5.08/5.14	10.74/10.25/10.93
PIO (Sp+Ob/Sp+St/Ob+St)	4.70/4.58/4.90	10.13/10.24/10.06
PIO (Sp+Ob+St/Sp+Ob+St+Euc.)	4.29/4.31	9.52/9.56

TABLE XV: Mean \pm standard deviation of classification error (%) are given for results obtained using SENet-Resnet-101, and 110-layer Resnets with constant depth (RCD) on Cifar-100.

Model Cifar-100 with DA (110 layer RCD)	Error
Euc. †	27.01 \pm 0.47
St	25.39 \pm 0.40
POMs of St	25.18 \pm 0.34
PIO (Sp+Ob+St)	23.96 \pm 0.28
PIO (Sp+Ob+St+Euc.)	23.79 \pm 0.15
(Additional results) Cifar-100 with DA (SENet-Resnet-101)	Error
Euc. †	19.93 \pm 0.51
PIO (Sp+Ob+St)	18.96 \pm 0.27
PIO (Sp+Ob+St+Euc.)	18.54 \pm 0.16

B. Comparison with Vanilla Network Ensembles

Our method fundamentally differs from network ensembles. In order to analyze the results for network ensembles of CNNs, we employed an ensemble method [44] by *voting of decisions* of Resnet 44 on Cifar 10. When CNNs trained on individual Euc, Sp, Ob, and St are ensembled using voting, we obtained 7.02% (Euc+Sp+Ob+St) and 6.85% (Sp+Ob+St) errors (see Table 1 for comparison). In our analyses of ensembles (PI, PO and PIO), each POM contains $\frac{N_l}{M}$ weights, where N_l is the number of weights used at the l^{th} layer, and M is the number of POMs. When each CNN in the ensemble was trained using an individual manifold which contains $\frac{1}{4}$ of weights (using $M = 4$ as utilized in our experiments), then we obtained 11.02% (Euc), 7.76% (Sp), 7.30% (Ob), 7.18% (St), 9.44% (Euc+Sp+Ob+St) and 7.05% (Sp+Ob+St) errors. Thus, our proposed methods outperform ensembles constructed by voting.

C. Analyses for Larger DNNs with Large Scale Image Datasets

We give the results for Cifar-100 obtained using data augmentation denoted by with DA in Table XV. Cifar-100 dataset consist of 5×10^4 training and 10^4 test images belonging to 100 classes.

In Table XV, we provide results using the state-of-the-art Squeeze-and-Excitation (SE) blocks [37] implemented for Resnets with 110 layers (Resnet-110) on Cifar-100. We run the experiments 3 times and provide the average performance.

TABLE XVI: Analysis of classification error (%) of state-of-the-art DNNs which employ separable convolutions on Imagenet dataset.

Model	Classification Error
Resnext-50 (Euc. [19])	22.2
Resnext-50 (Euc. †)	22.7
Resnext-50 (Euc.WSS)	22.3
Resnext-50 (PIO-SOSE)	21.5
Resnext-50 (PIO-SOSE-WSS)	21.3
Mobilenetv2 (Euc. [20])	28.0
Mobilenetv2 (Euc. †)	27.9
Mobilenetv2 (Euc.-WSS)	27.5
Mobilenetv2 (PIO-SOSE)	26.8
Mobilenetv2 (PIO-SOSE-WSS)	26.4
DeepRoots (Euc. [21])	26.6
DeepRoots (Euc. †)	27.0
DeepRoots (Euc.-WSS)	26.6
DeepRoots (PIO-SOSE)	25.9
DeepRoots (PIO-SOSE-WSS)	25.5

In the second set of experiments, we perform separable convolution operations using the proposed weight splitting scheme. We compare the results using various popular separable convolution schemes, such as depth-wise and channel-wise convolution implemented using state-of-the-art DNNs such as ResNext with 50 layers (ResNext-50) [19], MobileNet v2 with 21 layers (Mobilenet) [20] and 50 layer Resnets with hierarchical filtering using 4 roots (DeepRoots) [21]. The results obtained using PIO with (Sp+Ob+St+Euc.) with the separable convolution scheme proposed in the corresponding related work are denoted by PIO-SOSE. The results obtained using PIO with (Sp+Ob+St+Euc.) with our proposed WSS are denoted by PIO-SOSE-WSS.

REFERENCES

- [1] Chiyuan Zhang, Samy Bengio, Moritz Hardt, Benjamin Recht, and Oriol Vinyals. Understanding deep learning requires rethinking generalization. In *Proc. of the 5th Int. Conf. on Learn. Rep. (ICLR)*, 2017.
- [2] Behnam Neyshabur, Srinadh Bhojanapalli, David Mcallester, and Nati Srebro. Exploring generalization in deep learning. In *Advances in Neural Information Processing Systems (NIPS)*, pages 5947–5956. 2017.
- [3] Peter L Bartlett, Dylan J Foster, and Matus J Telgarsky. Spectrally-normalized margin bounds for neural networks. In *Advances in Neural Information Processing Systems (NIPS)*, pages 6240–6249. 2017.
- [4] Taiji Suzuki. Fast generalization error bound of deep learning from a kernel perspective. In *Proc. of the 21st Int. Conf. on Artificial Intelligence and Statistics (AISTATS)*, volume 84, pages 1397–1406, 2018.
- [5] Pan Zhou and Jiashi Feng. Understanding generalization and optimization performance of deep CNNs. In *Proc. of the 35th Int. Conf. on Mach. Learn. (ICML)*, volume 80, pages 5960–5969, 2018.
- [6] Sanjeev Arora, Rong Ge, Behnam Neyshabur, and Yi Zhang. Stronger generalization bounds for deep nets via a compression approach. In *Proc. of the 35th Int. Conf. on Mach. Learn. (ICML)*, volume 80, pages 254–263, 2018.
- [7] Noah Golowich, Alexander Rakhlin, and Ohad Shamir. Size-independent sample complexity of neural networks. In *Proc. of the 31st Conf. on Learning Theory (COLT)*, pages 297–299. 2018.
- [8] Behnam Neyshabur, Srinadh Bhojanapalli, and Nathan Srebro. A PAC-bayesian approach to spectrally-normalized margin bounds for neural networks. In *Proc. of the 6th Int. Conf. on Learn. Rep. (ICLR)*, 2018.
- [9] Martin Anthony and Peter L. Bartlett. *Neural Network Learning: Theoretical Foundations*. Cambridge University Press, New York, NY, USA, 1st edition, 2009.
- [10] Sergey Ioffe and Christian Szegedy. Batch normalization: Accelerating deep network training by reducing internal covariate shift. In *Proc. of the 35th Int. Conf. on Mach. Learn. (ICML)*, pages 448–456, 2015.
- [11] Bo Xie, Yingyu Liang, and Le Song. Diverse Neural Network Learns True Target Functions. In *Proc. of the 20th Int. Conf. on Artificial Intelligence and Statistics (AISTATS)*, volume 54, pages 1216–1224, 2017.
- [12] Shibani Santurkar, Dimitris Tsipras, Andrew Ilyas, and Aleksander Madry. How does batch normalization help optimization? (no, it is not about internal covariate shift). In *Advances in Neural Information Processing Systems (NIPS)*. 2018.
- [13] Mete Ozay and Takayuki Okatani. Training cnns with normalized kernels. In *AAAI Conference on Artificial Intelligence*, 2018.
- [14] Haoran Chen, Yanfeng Sun, Junbin Gao, Yongli Hu, and Baocai Yin. Partial least squares regression on riemannian manifolds and its application in classifications. *CoRR*, abs/1609.06434, 2016.
- [15] Yui Man Lui. Human gesture recognition on product manifolds. *J. Mach. Learn. Res.*, 13(1):3297–3321, Nov 2012.

- [16] Minhyung Cho and Jaehyung Lee. Riemannian approach to batch normalization. In *Advances in Neural Information Processing Systems (NIPS)*, 2017.
- [17] Tim Salimans and Diederik P. Kingma. Weight normalization: A simple reparameterization to accelerate training of deep neural networks. In *Advances in Neural Information Processing Systems (NIPS)*, 2016.
- [18] Minhyung Cho and Jaehyung Lee. Riemannian approach to batch normalization. In *Advances in Neural Information Processing Systems (NIPS)*, pages 5231–5241. 2017.
- [19] Saining Xie, Ross Girshick, Piotr Dollar, Zhuowen Tu, and Kaiming He. Aggregated residual transformations for deep neural networks. In *IEEE Int. Conf. on Comp. Vis. Patt. Recog. (CVPR)*, July 2017.
- [20] Mark Sandler, Andrew Howard, Menglong Zhu, Andrey Zhmoginov, and Liang-Chieh Chen. Mobilenetv2: Inverted residuals and linear bottlenecks. In *IEEE Int. Conf. on Comp. Vis. Patt. Recog. (CVPR)*, June 2018.
- [21] Yani Ioannou, Duncan Robertson, Roberto Cipolla, and Antonio Criminisi. Deep roots: Improving cnn efficiency with hierarchical filter groups. In *IEEE Int. Conf. on Comp. Vis. Patt. Recog. (CVPR)*, July 2017.
- [22] Behnam Neyshabur, Ryota Tomioka, and Nathan Srebro. Norm-based capacity control in neural networks. In *Proc. of the 28th Conf. on Learning Theory (COLT)*, volume 40, pages 1376–1401, 2015.
- [23] Z. D. Bai and Y. Q. Yin. Limit of the smallest eigenvalue of a large dimensional sample covariance matrix. *The Annals of Probability*, 21(3):1275–1294, 07 1993.
- [24] Z. D Bai, Jack W Silverstein, and Y.Q Yin. A note on the largest eigenvalue of a large dimensional sample covariance matrix. *Journal of Multivariate Analysis*, 26(2):166 – 168, 1988.
- [25] Xavier Glorot and Yoshua Bengio. Understanding the difficulty of training deep feedforward neural networks. In *Proc. of the 13th Int. Conf. on Artificial Intelligence and Statistics (AISTATS)*, volume 9, pages 249–256, 2010.
- [26] P. A. Absil and Jerome Malick. Projection-like retractions on matrix manifolds. *SIAM Journal on Optimization*, 22(1):135–158, 2012.
- [27] Kenji Kawaguchi. Deep learning without poor local minima. In D. D. Lee, M. Sugiyama, U. V. Luxburg, I. Guyon, and R. Garnett, editors, *Advances in Neural Information Processing Systems (NIPS)*, pages 586–594. 2016.
- [28] Alon Brutzkus and Amir Globerson. Globally optimal gradient descent for a convnet with gaussian inputs. In *Proc. of the 34th Int. Conf. on Mach. Learn. (ICML)*, pages 605–614, 2017.
- [29] Simon S. Du, Jason D. Lee, Yuandong Tian, Barnabás Póczos, and Aarti Singh. Gradient descent learns one-hidden-layer cnn: Don’t be afraid of spurious local minima. In *Proc. of the 35th Int. Conf. on Mach. Learn. (ICML)*, 2018.
- [30] Simon S. Du and Jason D. Lee. On the power of over-parametrization in neural networks with quadratic activation. In *Proc. of the 35th Int. Conf. on Mach. Learn. (ICML)*, 2018.
- [31] Chulhee Yun, Suvrit Sra, and Ali Jadbabaie. Global optimality conditions for deep neural networks. In *Proc. of the 6th Int. Conf. on Learn. Rep. (ICLR)*, 2018.
- [32] Moritz Hardt and Tengyu Ma. Identity matters in deep learning. In *Proc. of the 5th Int. Conf. on Learn. Rep. (ICLR)*, 2017.
- [33] Rong Ge, Jason D. Lee, and Tengyu Ma. Learning one-hidden-layer neural networks with landscape design. In *Proc. of the 5th Int. Conf. on Learn. Rep. (ICLR)*, 2017.
- [34] Chulhee Yun, Suvrit Sra, and Ali Jadbabaie. A critical view of global optimality in deep learning. *CoRR*, abs/1802.03487, 2018.
- [35] Maithra Raghu, Ben Poole, Jon Kleinberg, Surya Ganguli, and Jascha Sohl-Dickstein. On the expressive power of deep neural networks. In *Proc. of the 34th Int. Conf. on Mach. Learn. (ICML)*, volume 70, pages 2847–2854, 2017.
- [36] Quynh Nguyen and Matthias Hein. The loss surface of deep and wide neural networks. In *Proc. of the 34th Int. Conf. on Mach. Learn. (ICML)*, volume 70, pages 2603–2612, 2017.
- [37] Jie Hu, Li Shen, and Gang Sun. Squeeze-and-excitation networks. In *Proc. IEEE Conf. Comp. Vis. Patt. Recog. (CVPR)*, 2018.
- [38] Sergey Ioffe and Christian Szegedy. Batch normalization: Accelerating deep network training by reducing internal covariate shift. In *Proc. of the 32nd Int. Conf. Mach. Learn.*, volume 37, pages 448–456, 2015.
- [39] J.M. Lee. *Manifolds and Differential Geometry*. Graduate studies in mathematics. American Mathematical Society, 2009.
- [40] P. Petersen. *Riemannian Geometry*. Graduate Texts in Mathematics. Springer New York, 2006.
- [41] S. Bonnabel. Stochastic gradient descent on riemannian manifolds. *IEEE Trans. Autom. Control*, 58(9):2217–2229, Sept 2013.
- [42] Donald L. Fisk. Quasi-martingales. *Transactions of the American Mathematical Society*, 120(3):369–389, 1965.
- [43] Alex Krizhevsky, Ilya Sutskever, and Geoffrey E. Hinton. Imagenet classification with deep convolutional neural networks. In *Advances in Neural Information Processing Systems (NIPS)*, pages 1097–1105, 2012.
- [44] Kaiming He, Xiangyu Zhang, Shaoqing Ren, and Jian Sun. Deep residual learning for image recognition. In *IEEE Int. Conf. on Comp. Vis. Patt. Recog. (CVPR)*, 2016.
- [45] Yann Lecun, Yoshua Bengio, and Geoffrey Hinton. Deep learning. *Nature*, 521(7553):436–444, 5 2015.
- [46] Thomas H. Cormen, Charles E. Leiserson, Ronald L. Rivest, and Clifford Stein. *Introduction to Algorithm*. The MIT Press, 3rd edition, 2009.
- [47] Nicholas J. Higham. The scaling and squaring method for the matrix exponential revisited. *SIAM J. Matrix Anal. Appl.*, 26(4):1179–1193, Apr 2005.
- [48] C. S. Kenney and A. J. Laub. A schur–fréchet algorithm for computing the logarithm and exponential of a matrix. *SIAM Journal on Matrix Analysis and Applications*, 19(3):640–663, 1998.
- [49] Cleve Moler and Charles Van Loan. Nineteen dubious ways to compute the exponential of a matrix, twenty-five years later. *SIAM Review*, 45(1):3–49, 2003.
- [50] G.H. Golub and C.F. Van Loan. *Matrix computations*. Johns Hopkins University Press, Baltimore, MD, 2013.
- [51] Franklin T. Luk. A rotation method for computing the qr-decomposition. *SIAM Journal on Scientific and Statistical Computing*, 7(2):452–459, 1986.
- [52] Ian Masliah, Ahmad Ahmad, Azzam Haidar, Stanimire Tomov, Joël Falcou, and Jack Dongarra. High-performance matrix-matrix multiplications of very small matrices. In *22nd Int. European Conf. on Parallel and Dist. Comp. (Euro-Par’16)*, Grenoble, France, Aug 2016. Springer International Publishing.

- [53] Jack Dongarra, Mark Gates, Azzam Haidar, Jakub Kurzak, Piotr Luszczek, Stanimire Tomov, and Ichitaro Yamazaki. Accelerating numerical dense linear algebra calculations with gpus. *Numerical Computations with GPUs*, pages 1–26, 2014.
- [54] Stanimire Tomov, Jack Dongarra, and Marc Baboulin. Towards dense linear algebra for hybrid GPU accelerated manycore systems. *Parallel Computing*, 36(5-6):232–240, Jun 2010.
- [55] Stanimire Tomov, Rajib Nath, Hatem Ltaief, and Jack Dongarra. Dense linear algebra solvers for multicore with GPU accelerators. In *IPDPS*, pages 1–8, Atlanta, GA, April 19-23 2010. IEEE Computer Society.
- [56] Rajib Nath, Stanimire Tomov, and Jack Dongarra. Accelerating GPU kernels for dense linear algebra. In *VECPAR*, Berkeley, CA, June 22-25 2010. Springer.
- [57] Rajib Nath, Stanimire Tomov, and Jack Dongarra. An Improved MAGMA GEMM For Fermi Graphics Processing Units. *Int. J. High Perform. Comput. Appl.*, 24(4):511–515, November 2010.
- [58] William J. Brouwer and Pierre-Yves Taunay. *Efficient Batch LU and QR Decomposition on GPU*, pages 69–86. Springer International Publishing, 2014.
- [59] P. A. Absil and K. A. Gallivan. Joint diagonalization on the oblique manifold for independent component analysis. In *Proc. 31st IEEE Int. Conf. Acoust., Speech Signal Process.*, volume 5, pages 945–948, Toulouse, France, May 2006.
- [60] P.-A. Absil, R. Mahony, and R. Sepulchre. *Optimization Algorithms on Matrix Manifolds*. PUP, Princeton, NJ, USA, 2007.
- [61] Gao Huang, Yu Sun, Zhuang Liu, Daniel Sedra, and Kilian Q. Weinberger. Deep networks with stochastic depth. In *Proc. of the 14th European Conf. Comp. Vis.*, pages 646–661, Amsterdam, The Netherlands, 2016.
- [62] Christian Szegedy, Wei Liu, Yangqing Jia, Pierre Sermanet, Scott Reed, Dragomir Anguelov, Dumitru Erhan, Vincent Vanhoucke, and Andrew Rabinovich. Going deeper with convolutions. In *Proc. IEEE Conf. Comp. Vis. Patt. Recog.*, 2015.
- [63] Andrew G. Howard. Some improvements on deep convolutional neural network based image classification. *CoRR*, abs/1312.5402, 2013.
- [64] Ilya Sutskever, James Martens, George Dahl, and Geoffrey Hinton. On the importance of initialization and momentum in deep learning. In *Proc. Int. Conf. Mach. Learn.*, volume 28, pages 1139–1147, May 2013.
- [65] Mete Ozay and Takayuki Okatani. Optimization on submanifolds of convolution kernels in cnns. *CoRR*, abs/1610.07008, 2016.
- [66] Gao Huang, Zhuang Liu, and Kilian Q. Weinberger. Densely connected convolutional networks. In *Proc. IEEE Conf. Comp. Vis. Patt. Recog. (CVPR)*, 2017.